Mathematics and Systems Science 2025, 3(1), 3058.
https://doi.org/10.54517/mss3058

Article

Dynamics of a nonlinear multilayer beam structure on elastic foundation: Chaos detection and application to transport engineering technologies

Roger Eno[1], Martine Limi Wokwenmendam[2], Guy Bertrand Ndombou[3], Hervé Simo[4], Fabien Kenmogne[5,*], Sévérin Nguiya[3,6]

[1] Laboratory for Mechanics and Materials (LMM), National higher polytechnic School, The University of Douala, Douala 2701, Cameroon
[2] Department of Mechanical and Industrial Engineering, National high polytechnic institute (NAHPI), The university of Bamenda (UBa), Bambili 39, Cameroon
[3] Department of Common Trunk, National higher polytechnic School, The University of Douala, Douala 2701, Cameroon
[4] Department of Mechanical Engineering, the University institute of Technology, The University of Ngaoundéré, Ngaoundéré 455, Cameroon
[5] Department of Civil Engineering, Advanced Teacher Training College of the Technical Education, The University of Douala, Douala 1872, Cameroon
[6] Laboratory for Geophysics (LG), National higher polytechnic School, The University of Douala, Douala 2701, Cameroon
*** Corresponding author:** Fabien Kenmogne, kenfabien@yahoo.fr

CITATION

Eno R, Wokwenmendam ML, Ndombou GB, et al. Dynamics of a nonlinear multilayer beam structure on elastic foundation: Chaos detection and application to transport engineering technologies. Mathematics and Systems Science. 2025; 3(1): 3058. https://doi.org/10.54517/mss3058

ARTICLE INFO

Received: 11 November 2024
Accepted: 25 December 2024
Available online: 2 January 2025

Abstract: The dynamics of a composite consisting of the nonlinear multilayer beam structure, interacting through elastic intermediate layers, under mobile point loading is investigated. This study finds a direct application in transport engineering technologies, more precisely in railways, where the moving point load is the train, and the multilayer beam, the rails interacting with the ballast, the foundation and base layers. From the Lagrange formulations, the system of damping partial differential equations of the model is found, and by considering the non-dissipative case with weak nonlinearity and constant charge they are used to find the eigen modes and the natural vibration frequencies of the system. Then the dissipative case with nonlinearity is studied, with a particular attention carried on the temporal part, which is reduced to a system of coupled nonlinear differential equations, where the first line is forced. This system of equation is used to determine the equilibrium points, after which they are subsequently solved analytically through the multiple time scale method for harmonic resonance case, showing the formation of hysteresis more and more complex as the number of cells increases. The coupled nonlinear equations of the system is next solved numerically, with the transition of the system towards chaos analyzed through the bifurcation diagram and the maximum Lyapunov exponent, which show strong sensitivity to the coupling parameter λ_2 as well as the system frequency. The results show for $N = 2$ and for some parameters the periodic behavior and the crisis for $\omega = 0.5$. When the frequency is low; that is $\omega = 0.05$ the chaotic band is considerably reduced, chaos appearing around the nonlinearity parameter $\gamma_2 = 0.5$ and also for $\gamma_2 > 0.85$. The time trace shows chaotic pulses and bursting type behavior, for some choices of the coupling parameter. The synchronization curves are also plotted and it is shown that q_2 doesn't synchronizes with q_1 for some frequencies, while for others parameters, they synchronize, but fairly. For $N = 3$, the dynamics is more complex and the time traces plots show regular impulse for $\omega = 0.5$ and bursting for weak frequency, $\omega = 0.05$.

Keywords: multilayer beam structure; coupled of partial differential equation; mobile point load; hysteresis; chaotic impulse; bursting signal

1. Introduction

Structural design is an essential aspect of any construction project, and it involves a range of considerations that must be carefully evaluated to ensure the safety and stability of the structure [1]. One of the most critical factors in structural design is load-bearing capacity, which refers to the maximum weight that a structure can support without collapsing or experiencing significant damage. Load-bearing capacity determines the ability of a structure to support its own weight and any additional loads placed upon it. Structures are generally faced with various types of loads, among which are static and variable (moving) loads. Although the modeling of static loading for linear cases is well-established, ensuring the bearing capacity of structures in the face of moving loads is one of the engineering challenges, particularly in the design of buildings, bridges, and roads [2]. Load modeling in nonlinear structures, particularly incorporating large deformations, differs significantly from the treatment in linear analysis.

The study of nonlinear systems has been the subject of numerous studies in recent years [3]. This is due to the fact that nonlinearity finds its applications in several fields of physics and engineering, including mechanics [4], electronics [5,6], optics [7,8], civil engineering, and other related fields [9,10]. Note that unlike linear systems where the effects and causes are proportional quantities, in the nonlinear systems, the effects are nonlinear functions of the causes. For example, in nonlinear electronics, electrical voltages are nonlinear functions of currents [11]. In nonlinear mechanics, on the other hand, the tensions (or restoring forces) are nonlinear functions of the elongations [12,13]. In civil engineering in general and particularly in geotechnics, the displacements of elastic soils under foundations subjected to loading are nonlinear functions of displacements [14]. The consideration of nonlinearity in the study of systems is very important, as long as it allows us to understand certain phenomena observed experimentally in physical systems, such as the appearance of chaos and patterns formation, and to predict new ones [15–17], and especially it allows us to design devices to attenuate chaos. Nonlinearity thus allows justifying the chaotic or random behavior of certain systems, chaos being harmful for some systems and desirable for others. In telecommunications, chaos allows the masking and securing of information. In civil engineering, the sieves that vibrate chaotically have a higher yield [18]. It has been proven that although systems with one degree of freedom are dynamically rich, system dynamics become increasingly rich and complex as the degree of freedom becomes larger, whether these systems are linear or not. In civil engineering, and more particularly in the case of beams, the superposition of layers of intermediate beams allows for increasingly complex vibration modes. This is why in 2021, Jiang et al. [19] studied a multilayer structure consisting of a certain number of beams, interconnected and where the upper beam is subjected to loading. In this work they studied the dynamics and stability of this structure; however, they ignored the nonlinear behavior of this structure, which could provide significant results.

Beams on an elastic foundation, or columns and piles supported along their entire length, usually by the ground, are a well-known problem in structural mechanics [20,21], in addition to being a very common structural element, with applications in many engineering fields such as civil, mechanical, and offshore engineering, particularly in foundation analysis and design. The study of this structural configuration began with the pioneer works of Winkler [22] and has been addressed by many researchers with various theoretical tools, including numerical methods [23,24], finite element methods [25], analytical [26,27], and disturbance [28]. The linear behavior of beams on elastic foundations has been widely studied. However, little attention has been paid to their behavior in the nonlinear domain. In [20], Diego Froio et al. investigated the dynamics of a beam on a bilinear elastic foundation under harmonic moving load, in which they considered the effect of nonlinearity and neglected the dissipation. In their work, they didn't emphasize the prediction of chaos in their systems. In many important applications, the elastic foundation is the floor, which is generally very nonlinear. One can enumerate the work of Anas Ouzizi et al. [21], who investigated the nonlinear dynamics of beams on nonlinear fractional viscoelastic foundations subjected to moving loads with variable speeds. Thus, the nonlinear effect considerably influences the behavior of the beam by modifying its bearing capacity and its natural frequencies. In the present work, we consider the multilayer beam on an elastic foundation, as is the case in [19], and we consider the dissipation effects and carry an emphasis on the chaotic behavior by using analytical and numerical methods, which is new in what concerns the multilayer beam on an elastic foundation. Moreover, we take into account the dissipations, which can considerably affect the results as compared to previous ones, and we show that the dynamics of the system are very complex, depending on the nonlinearity and the nature of the coupling.

The main objective of this work is the dynamic analysis of a nonlinear multilayer beam structure under moving load.

The specific objectives are:

- Modeling of the system equation taking into account dissipation and nonlinearity;
- Study the stability of the nonlinear system;
- Check whether the system is regular or chaotic.

2. Model description and governing equations

2.1. Model description

We consider in this work the system of multilayer beams consisting of a set of beams interacting through elastic intermediate layers as presented in **Figure 1**. The first beam, subjected to a moving load with mass M moving with and speed V, constitutes the entrance to the system, while the foundation constitutes the system output. Let us outline that in railway engineering, this beam can be seen as the rails, and moving load, the motion of the train. The rails are laid on multilayer elastic soil through the ballasts. The motion of a train on bridges, in [29,30], could constitute another example. The simulation of high axial speed machining processes during milling operations and internal fluid flow in piping systems resting on a ground foundation is another example. In addition, the shafts of rotating machines resting on elastic supports (journal bearings) and floating in an industrial lubricant can be modeled as beams on a viscoelastic foundation [31,32]. The particle with mass M in **Figure 1** can also represent a heavy car on a bridge having several layers or a compactor working on a moving road [33], the road having several layers that interact with each other.

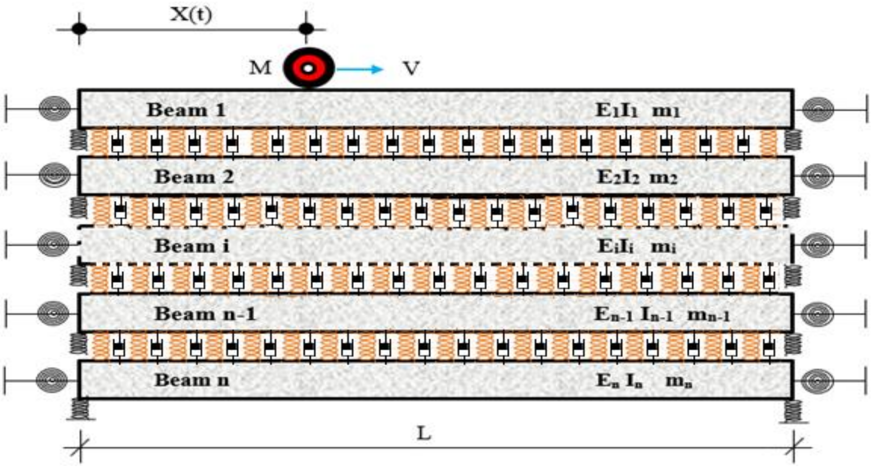

Figure 1. Multilayer beams consisting of a set of beams interacting through elastic intermediate layers; the first beam, subjected to a moving load with speed V.

2.2. Lagrange equation of the network

Let us consider here the network as shown in **Figure 1**, which is composed of n layers on an elastic foundation and therefore $n-1$ interconnections over the length l, in which the layers can relatively move to each other depending on the properties of the interconnections. Thus, the system will have the following energies:

2.2.1. Kinetic energy

The rotational inertia of the beam will be neglected because the beam is slender. Then the kinetic energy is given by the following Equation (1) [16,34]:

$$T = \frac{1}{2}\sum_{i=1}^{N} \rho_i A_i \int_0^L \left(\frac{\partial w_i(x,t)}{\partial t}\right)^2 dx \tag{1}$$

where ρ_i is the density of the material at position i, A_i is the cross section of the i^{th} beam, L is the length of the beam, and $w_i = w_i(\mathrm{x}, \mathrm{t})$ i is the transverse displacement of the beam (in one direction) at position x, The Winkler soil model will be used here, which assumes that the displacement only appears in the loaded zone and, outside this zone, the deflections are zero [16,35,36]. With $\rho_i A_i = m_i$, which is the elementary mass of i^{th} position.

2.2.2. Potential energy

- Bending potential energy for the i^{th} particle

The potential energy due to bending can be evaluated as follows [34]:

$$V_{\text{bend}} = \frac{1}{2}\sum_{i=1}^{N} E_{fi} I_i \int_0^L \left(\frac{\partial^2 w_i(x,t)}{\partial x^2}\right)^2 dx \tag{2}$$

where Ef_i is the Young's modulus of the i^{th} beam.

- Potential energy due to coupling

It can be evaluated using the following equation, in which it is assumed that the motion of railway located at position i is affected by all neighbors located, at position j.

$$V_c = \frac{1}{2}\sum_{i=1}^{N}\gamma_i\sum_{j=1}^{N}\int_0^L \left(w_i(x,t) - w_j(x,t)\right)^2 dx \tag{3}$$

where γ_i is the coupling coefficient, where the value can be experimentally found from the measured input–output data, although, it is not done in this work.

- Stretching potential energy [34]

$$V_{Stretch} = \frac{1}{2}\sum_{i=1}^{N}\frac{E_i A_0}{2L_i}\left(\frac{1}{2}\int_0^L\left(\frac{\partial w_i(x,t)}{\partial x}\right)^2 dx\right)^2 \tag{4}$$

In which the Li are equal for all beams.

- Elastic potential energy [34]

$$V_{found} = \frac{1}{2}\sum_{i=1}^{N}\int_0^L K_{fi}\left(w_i(x,t)\right)^2 dx \tag{5}$$

- Potential energy due to loadings

Let us assume that the loading, applied at position x_0, by mobile moving with speed V, such as $x_0 = Vt$. The potential energy is then given by [34]:

$$V_{load} = -\sum_{i=1}^{N}\int_0^L P(x,t)\omega_i(x,t)dx \tag{6}$$

where $P(x,t) = P_0\delta(x - \mathrm{x}_0)\delta(j - i)$, $P_0 = Mg$ is the weight of the moving load located on the first layer, and g is the intensity of gravity, while δ is the Dirac delta function.

With

$$\delta(x - x_0) = \begin{cases} 1 \; if \; x = x_0 \\ 0 \; else \end{cases} \tag{7}$$

2.2.3. Lagrangian equation

The Lagrangian of the network is defined as follows [16,34]

$$L = T - \left(V_{\mathrm{bend}} + V_c + V_{Strestch} + V_{found} + V_{load}\right) \tag{8}$$

leading to

$$\begin{aligned} L = \frac{1}{2}\sum_{i=1}^{N}\int_0^L dx \Bigg[\rho_i A_i\left(\frac{\partial w_i(x,t)}{\partial t}\right)^2 - E_{fi}I_i\left(\frac{\partial^2 w_i(x,t)}{\partial x^2}\right)^2 - K_{fi}\left(w_i(x,t)\right)^2 \\ + 2P_0 w_i(x,t)\delta(x - \mathrm{x}_0)\delta(j - i) + \gamma_i\sum_{j=1}^{M}\left(w_i(x,t) - w_j(x,t)\right)^2\Bigg] \\ - \sum_{i=1}^{N}\frac{E_i A_{0\mathrm{i}}}{2L_i}\left(\frac{1}{2}\int_0^L\left(\frac{\partial w_i(x,t)}{\partial x}\right)^2 dx\right)^2 \end{aligned} \tag{9}$$

Taking into account that in physical systems anything cannot vibrate indefinitely, the dissipation (loss introduced by the friction) is introduced in the system by the Rayleigh dissipation function and is then given as [34]:

$$D = \frac{1}{2}\sum_{i=1}^{N} \mu_i \int_0^L \left(\frac{\partial w_i(x,t)}{\partial t}\right)^2 \tag{10}$$

which allows us to define the equations of motion in the form [16,34]:

$$\frac{\partial}{\partial t}\left(\frac{\partial L}{\partial w_{it}}\right) - \frac{\partial L}{\partial \omega_i} + \frac{\partial}{\partial x}\left(\frac{\partial L}{\partial w_{ix}}\right) - \frac{\partial^2}{\partial x^2}\left(\frac{\partial L}{\partial w_{ixx}}\right) = -\frac{\partial D}{\partial w_{it}} \tag{11}$$

2.3. Equations of motion for the non-dissipative case and with weak nonlinearity

2.3.1. Set of partial differential equations of motion

For this particular case, we consider that the system is loaded with continuum charge, meaning that $P(x,t) = q_0 L\delta(i-1)$, and for this particular case with $D = E_i A_0 = 0$, Equation (11) leads to

$$m_i w_{itt} + K_{fi} w_i + \gamma_i \sum_{i-1}^{N} (w_i - w_j) + E_{fi} I_i \, w_{ixx} - p(x,t)\delta(i-1) = 0 \tag{12}$$

With $\rho_i A_i = m_i$which allows to have the equation below in expanded form

$$\begin{cases} m_1 w_{1tt} + k\rho_1 w_1 + \gamma_1 \sum_{i-1}^{N} \left(w_1 - w_j\right) + E_{f1} I_1 w_{1xx} = q_0 L \\ m_2 w_{2tt} + k\rho_2 w_2 + \gamma_2 \sum_{j=1}^{M} (w_2 - w_j) + E_{f2} I_2 \, w_{2xx} = 0 \\ \quad \ldots \\ m_i w_{itt} + k\rho_i w_i + \gamma_i \sum_{j=1}^{M} (w_i - w_j) + E_{fi} I_i \, \omega_{ixx} = 0 \\ \quad \ldots \\ m_N w_{itt} + k\rho_N w_N + \gamma_N \sum_{j=1}^{M} (w_N - w_j) + E_{fN} I_N \, \omega_{Nxx} = 0 \end{cases} \tag{13}$$

2.3.2. Set of differential equations governing temporal part and solutions

Differential equations governing temporal part

Suppose that the system is a simply supported beam localized at position x_0, we have:

$$P(x,t) = P_0 \delta(x - x_0)\delta(i-1) \tag{14}$$

Let us seek the displacement by making the Fourier transform in the form $W_i(x,t) = \sum_{n=1}^{\infty} q_{ni}(t) \sin\left(\frac{n\pi}{l}x\right)$, subjected to loading to $P(x,t) = \sum_{n=1}^{\infty} c_0 \sin\left(\frac{n\pi}{l}x\right)$, with

$$C_0 = \frac{2}{L}\int_0^L P(x,t)\, sin\left(\frac{n\pi}{l}x\right) dx = \frac{2P_0}{L} sin\left(\frac{n\pi x_0}{L}\right) \tag{15}$$

leading to the following equation:

$$\begin{cases} m_1 q_{1tt} + \left(k\rho_1 - \frac{E_{f1} I_1 n^2 \pi^2}{L^2}\right) q_1 + \gamma_1 \sum_{j=1}^{N} (q_1 - q_j) = \frac{2q_0}{L} sin\left(\frac{n\pi x_0}{L}\right) \\ m_2 q_{2tt} + \left(k\rho_2 - \frac{E_{f2} I_2 n^2 \pi^2}{L^2}\right) q_2 + \gamma_2 \sum_{j=1}^{N} (q_2 - q_j) = 0 \\ \dots . \\ \dots . \\ \dots . \\ m_N q_{Ntt} + \left(k\rho_N - \frac{E_{fN} I_N n^2 \pi^2}{L^2}\right) q_N + \gamma_N \sum_{j=1}^{N} (q_N - q_j) = 0 \end{cases} \quad (16)$$

Stationary solutions

The stationary solution is obtained whether $q_{itt} = 0$,, leading to the algebraic equation $AQ = B$, with $Q = (q_1, q_2, q_3, \dots, q_n)$, $B = \left[\frac{2}{L} P_0 sin\left(\frac{n\pi}{L} x_0\right), 0, 0, 0, \dots ., 0\right]$, and

$$A = \begin{vmatrix} \Gamma_1 & -\gamma_1 & -\gamma_1 & \dots . & -\gamma_1 \\ -\gamma_2 & \Gamma_2 & -\gamma_2 & \dots . & -\gamma_2 \\ -\gamma_3 & -\gamma_3 & \Gamma_3 & \dots . & -\gamma_3 \\ \dots . & \dots . & \dots . & \dots . & \dots . \\ -\gamma_N & -\gamma_N & -\gamma_N & \dots . & \Gamma_N \end{vmatrix} \quad (17)$$

in which $\Gamma_i = k\rho_i - E_{fi} I_i \frac{n^2\pi^2}{l^2} + \gamma_i (N-1)$, leading to the solution $Q = {}^{B}\!/_{A}$. For the particular case where $N = 2$, the stationary solution of the system is in the form:

$$\begin{cases} q_1 = \frac{2P_0 \Gamma_2}{L(\Gamma_1\Gamma_2 - \gamma_1\gamma_2)} sin\left(\frac{n\pi}{L} x_0\right) \\ q_2 = \frac{2P_0 \gamma_2}{L(\Gamma_1\Gamma_2 - \gamma_1\gamma_2)} sin\left(\frac{n\pi}{L} x_0\right) \end{cases} \quad (18)$$

leading to

$$\begin{cases} w_1(x) = 2P_0 \sum_{n=1}^{N} \frac{\Gamma_2}{\mathrm{L}(\Gamma_1\Gamma_2 - \gamma_1\gamma_2)} sin\left(\frac{n\pi}{L} x_0\right) sin\left(\frac{n\pi}{L} x\right) \\ w_2(x) = 2P_0 \sum_{n=1}^{N} \frac{\gamma_2}{\mathrm{L}(\Gamma_1\Gamma_2 - \gamma_1\gamma_2)} sin\left(\frac{n\pi}{L} x_0\right) sin\left(\frac{n\pi}{L} x\right) \end{cases} \quad (19)$$

The transient homogeneous solution of the linear equation for the system is such as $\mathrm{q_i(t) = q_{0i} cos(\omega t + \phi_0)}$, leading to the following set of equations:

$$\left(-\mathrm{m_i}\omega^2 + \left(\mathrm{k}\rho_\mathrm{i} - \frac{E_{fi}\mathrm{I_i n^2 \pi^2}}{\mathrm{L^2}}\right) + \gamma_\mathrm{i}(\mathrm{N}-1)\right)\mathrm{q_i} - \gamma_\mathrm{i} \sum_{\mathrm{j \neq i}}^{\mathrm{N}} \mathrm{q_j} = 0, \text{ i} = 1, 2, \dots, \mathrm{N} \quad (20)$$

which can be rewritten in the following expansion form as $\mathrm{A_0 Q_{i0}} = 0$, with

$$A_0 = \begin{bmatrix} -m_1\omega^2+\Gamma_1 & -\gamma_1 & -\gamma_1 & .. & -\gamma_1 & -\gamma_1 \\ -\gamma_2 & -m_2\omega^2+\Gamma_2 & -\gamma_2 & .. & -\gamma_2 & -\gamma_2 \\ -\gamma_3 & -\gamma_3 & -m_3\omega^2+\Gamma_3 & .. & -\gamma_3 & -\gamma_3 \\ .. & .. & .. & .. & .. & .. \\ -\gamma_{N-1} & -\gamma_{N-1} & -\gamma_{N-1} & .. & -m_{N-1}\omega^2+\Gamma_{N-1} & -\gamma_{N-1} \\ -\gamma_N & -\gamma_N & -\gamma_N & .. & -\gamma_N & -m_N\omega^2+\Gamma_N \end{bmatrix} \tag{21}$$

The homogeneous Equation (20) has a non-trivial solution whether the determinant of Equation (21) is zero, leading to the dispersion relation

For *N* = 2, one has:

$$\omega^2 = \frac{1}{2}\left(\frac{m_1\Gamma_2 + m_2\Gamma_1 \pm \sqrt{(m_1\Gamma_2 - m_2\Gamma_1)^2 + 4m_1m_2\gamma_1\gamma_2}}{m_1m_2}\right) \tag{22}$$

which defines the frequency of each mode of vibration.

For *N* = 3, Let us introduce the following parameters:

$$\begin{aligned} p_0 &= \frac{\Gamma_1}{m_1} + \frac{\Gamma_2}{m_2} + \frac{\Gamma_3}{m_3} \\ p_1 &= \frac{\Gamma_2\Gamma_3 - \gamma_2\gamma_3}{m_2m_3} + \frac{\Gamma_1\Gamma_3 - \gamma_1\gamma_3}{m_1m_3} + \frac{\Gamma_2\Gamma_1 - \gamma_2\gamma_1}{m_1m_2} \\ p_2 &= \frac{2\gamma_1\gamma_2\gamma_3 - \Gamma_1\Gamma_2\Gamma_3 + \gamma_1\gamma_3\Gamma_2 + \gamma_1\gamma_2\Gamma_3 + \Gamma_1\gamma_2\gamma_3}{m_1m_2m_3} \\ P_{11} &= p_1 - \frac{1}{3}p_0^2 \\ p_{12} &= -\frac{2}{27}p_0^3 + p_2 + \frac{1}{3}p_0p_1 \end{aligned} \tag{23}$$

leading to the following characteristic frequency

$$\omega^2 = \frac{p_0}{3} + \frac{1}{3}\left(\frac{27p_{12}+3\sqrt{81p_{12}^2+12p_{11}^2}}{2}\right)^{1/3} \exp\left(\frac{2}{3}i\pi n\right) + \frac{1}{3}\left(\frac{27p_{12}-3\sqrt{81p_{12}^2+12p_{11}^2}}{2}\right)^{1/3} \exp\left(-\frac{2}{3}i\pi n\right), n=0,1,2. \tag{24}$$

2.4. Dissipative case with nonlinearity

2.4.1. Equation governing the temporal part of the system

Let us look for a solution with the standing wave in the form: $w_i(x,t) = \varphi_i(x)q_i(t)$, where $\varphi_i(x)$ is the spatial part viewed as the envelope and q_i the temporal part. By substituting this equation into Equation (8), one has the following expression of the Lagrangian:

$$L = \frac{1}{2}\sum_{i=1}^{N}\left[m_i\dot{q}_i^2(t)\int_0^L \varphi_i^2(x)dx - \left[E_{fi}I_i\int_0^L\left(\frac{\partial^2\varphi_i(x)}{\partial x^2}\right)^2 dx + K_{fi}\int_0^L \varphi_i^2(x)dx\right]q_i^2(t) \right.$$
$$- 2P_0 q_i(t)\int_0^L \varphi_i(x)\delta(x - v_e t)dx \tag{25}$$
$$\left. - \gamma_i\sum_{j=1}^{M}\left(q_i(t) - q_j(t)\right)^2\int_0^L \varphi_i(x)^2 dx - \frac{E_i A_{0i}}{4L_i}q_i^4(t)\left(\int_0^L\left(\frac{\partial\varphi_i(x)}{\partial x}\right)^2 dx\right)^2\right]$$

The dissipation function is then given by:

$$F_D = \frac{1}{2}\sum_{i=1}^{N}\mu_{ir}\,\dot{q}_i^2(t)\int_0^L \varphi_i^2(x)dx \tag{26}$$

The following Lagrangian equation can thus be used:

$$\frac{\partial}{\partial t}\left(\frac{\partial L}{\partial q_i}\right) - \frac{\partial L}{\partial q_i} = \frac{\partial F_D}{\partial \dot{q}_i} \tag{27}$$

Leading to the following damped equation of motion:

$$\ddot{q}_i + \mu_i\dot{q}_i + \omega_i^2 q_i(t) + \tilde{\gamma}_i\sum_{j=1}^{M}\left(q_i - q_j\right) + \lambda_i q_i^3 = F_i(t)\,\delta(i-1) \tag{28}$$

With

$$\mu_i = \frac{\mu_{ir}}{m_i};\ \omega_i^2 = \frac{1}{m_i}\left(E_{fi}I_i\frac{\int_0^L\left(\frac{\partial^2\varphi_i(x)}{\partial x^2}\right)^2 dx}{\int_0^L \varphi_i^2(x)dx} + k_{fi}\right)$$
$$\lambda_i = \frac{E_i A_{0i}}{2L_i m_i}\frac{\left(\int_0^L\left(\frac{\partial\varphi_i(x)}{\partial x}\right)^2 dx\right)^2}{\int_0^L \varphi_i^2(x)dx} \tag{29}$$
$$\tilde{\gamma}_i = \frac{\gamma_i}{m_i\int_0^L \varphi_i^2(x)dx}$$
$$F(t) = \frac{2P_0}{m_i\int_0^L \varphi_i^2(x)dx}\varphi_i(v_e t)$$

Equation (29) is the set of the coupled Duffing equations [37] with the influence of all neighbors, in which μ_i is the dissipation coefficient, and δ(1−*i*) is introduced since the load is applied only on the first layer and the other layers undergo. Note that the Duffing equations are generally used to describe the dynamic behavior of many real-world nonlinear systems for a wide range of frequency bands and amplitudes of the excitation signal in nonlinear sciences and engineering [33]. For example, the Duffing oscillator has been used successfully to model a variety of physical processes such as stiffening springs, buckling of beams, nonlinear electronic circuits, Josephson superconducting parametric amplifiers, and ionization waves in plasmas [38,39]. In the forced Duffing equation, the dissipation parameters are responsible for the formation of hysteresis in the amplitude-dependent frequency curves [38].

2.4.2. Equilibrium points

Let us look for the equilibrium points and then study the stability for the case with two and three layers in order to find the analytical solution of this equation. Equation (28) can thus be rewritten in the following form:

$$\begin{cases} \ddot{q}_1 + \mu_1\dot{q}_1 + \omega_1^2 q_1 + \lambda_1 q_1^3 + \gamma_1\left[(N-1)q_1 - \sum_{n\neq 1}^{N} q_n\right] = f(t) = \psi \\ \dots \\ \ddot{q}_2 + \mu_2\dot{q}_2 + \omega_2^2 q_2 + \lambda_2 q_2^3 + \gamma_2\left[(N-1)q_2 - \sum_{n\neq 2}^{N} q_n\right] = 0 \\ \dots \\ \ddot{q}_i + \mu_i\dot{q}_i + \omega_i^2 q_i + \lambda_i q_i^3 + \gamma_i\left[(N-1)q_i - \sum_{n\neq i}^{N} q_n\right] = 0 \\ \dots \\ \ddot{q}_N + \mu_N\dot{q}_N + \omega_N^2 q_N + \lambda_N q_N^3 + \gamma_N\left[(N-1)q_N - \sum_{n\neq N}^{N} q_n\right] = 0 \end{cases} \tag{30}$$

In order to find the equilibrium points for the particular case where one has only two layers, it is obvious that:

$$\begin{cases} \omega_1^2 q_1 + \gamma_1(q_1 - q_2) + \lambda_1 q_1 = F \\ \omega_2^2 q_2 + \gamma_2(q_2 - q_1) + \lambda_2 q_2^3 = 0 \end{cases} \tag{31}$$

In order to combine these two equations, one has, from the second line.

$$q_1 = \frac{(\omega_1^2 + \gamma_2)q_2 + \lambda_2 q_2^3}{\gamma_2} \tag{32}$$

Substituting q_1 into the first line of Equation (31) one has the polynomial Equation (33) of order 9, where one must vary the values of ω and plot to have the equilibrium points.

$$\begin{aligned} &\frac{\lambda_1\lambda_2^3}{\gamma_2^3} q_2^9 + \frac{3\lambda_1\lambda_2^2(\omega^2+\gamma_2)}{\gamma_2^3} q_2^7 + \frac{3\lambda_1\lambda_2(\omega^2+\gamma_2)^2}{\gamma_2^3} q_2^5 + \left(\frac{\omega^2\lambda_2}{\gamma_2} + \frac{\gamma_1\lambda_2}{\gamma_2} + \frac{\lambda_1(\omega^2+\gamma_2)^3}{\gamma_2^3}\right) q_2^3 \\ &\quad + \frac{\omega^2(\omega^2+\gamma_2+\gamma_1)}{\gamma_2} q_2 - F = 0 \end{aligned} \tag{33}$$

This equation is solved and plotted in **Figure 2**, which shows only one solution.

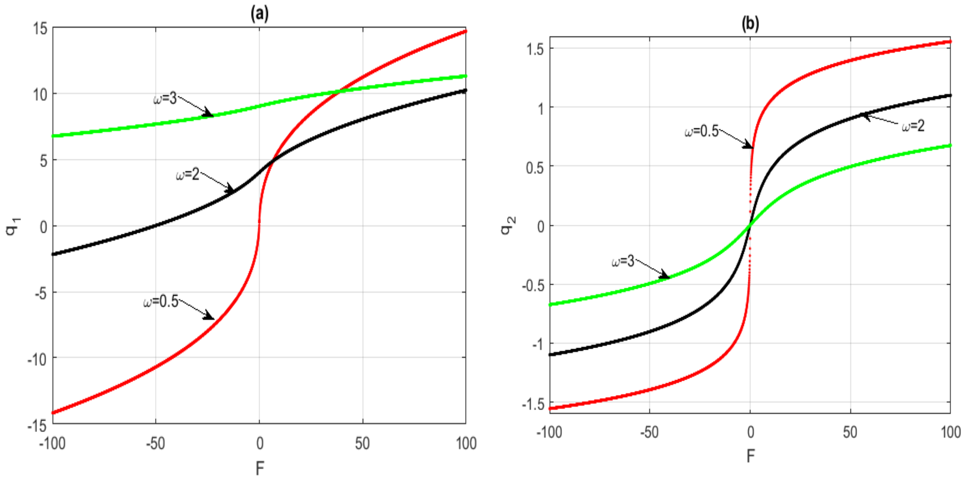

Figure 2. Equilibrium points for varying values of F and for: $\lambda_1 = 1$; $\lambda_2 = 1.5, \gamma_1 = 1, \gamma_2 = 2$; (**a**): q_1, (**b**): q_2. As one can see, only one solution is found.

3. Solutions of the damped case with nonlinearity

3.1. Analytical solutions

3.1.1. Solution for *N* = 2

Here, we will first make an emphasis on the case where N = 2, and the set of Equation (28) leads to:

$$\begin{cases} \ddot{q}_1 + \mu_1 \dot{q}_1 + \omega_1^2 q_1 + \gamma_1 (q_1 - q_2) + \lambda_1 q_1^3 = A\cos(\Omega t) \\ \ddot{q}_2 + \mu_2 \dot{q}_2 + \omega_2^2 q_2 + \gamma_2 (q_2 - q_1) + \lambda_2 q_2^3 = 0 \end{cases} \tag{34}$$

Let us introduce the small parameter $\varepsilon \ll 1$, such as $\mu_1 = \varepsilon\mu_{10}$, $\mu_2 = \varepsilon\mu_{20}$, $\lambda_1 = \varepsilon\lambda_{10}$, $\gamma_2 = \varepsilon\gamma_{20}$, $A = \varepsilon A_0$, $\gamma_1 = \varepsilon\gamma_{10}$, for harmonic resonance, and the variables

$$q_1 = \mathrm{q}_{10} + \varepsilon q_{11} + \cdots, q_2 = \mathrm{q}_{20} + \varepsilon q_{21} + \cdots, T_0 = t, T_1 = \varepsilon t, T_2 = \varepsilon^2 t, \ldots. \tag{35}$$

leading to:

$$\frac{d}{dt} = D_0 + \varepsilon D_1 + \varepsilon^2 D_2 + \cdots, D_0 = \frac{\partial}{\partial T_0}, D_1 = \frac{\partial}{\partial T_1}, D_2 = \frac{\partial}{\partial T_2}, \ldots \tag{36}$$

One obtains thus for:

- The equation at order ε^0,

$$D_0^2 q_{20} + \omega_2^2 q_{20} = 0, D_0^2 q_{10} + \omega_1^2 q_{10} = 0 \tag{37}$$

admitting as solutions:

$$q_{10} = R_1(T_1)\cos(\omega_1 T_0 - \phi_1(T_1)), q_{20} = R_2(T_1)\cos(\omega_2 T_0 - \phi_2(T_1)) \tag{38}$$

- The equation at order ε^1, leads to

$$\begin{aligned} D_0^2 q_{11} + \omega_1^2 q_{11} &= A_0 \cos(\Omega T_0) - \mu_{10} D_0 q_{10} - 2 D_0 D_1 q_{10} - \lambda_{10} q_{10}^3 \\ D_0^2 q_{21} + \omega_2^2 q_{21} &= -\mu_{20} D_0 q_{20} - 2 D_0 D_1 q_{20} - \lambda_{20} q_{20}^3 \end{aligned} \tag{39}$$

Introducing solution Equation (38) into Equation (39), one has the following coupled of equations

$$D_0^2 q_{11} + \omega_1^2 q_{11} = -\frac{1}{4}\lambda_{10} R_1^3 \cos(3\omega_1 T_0 - 3\phi_1) + \Big(-\omega_1(2D_1R_1 + \mu_{10}R_1)\sin(\phi_1) - \Big(2\omega_1 R_1 D_1\phi_1 + \gamma_{10}R_1 + \frac{3}{4}\lambda_{10}R_1^3\Big)\cos(\phi_1)\Big)\cos(\omega_1 T_0) + \gamma_{10}R_2\cos(\phi_2)\cos(\omega_2 T_0) + A_0\cos(\Omega T_0) + \Big(\omega_1(2D_1R_1 + \mu_{10}R_1)\cos(\phi_1) - \Big(2\omega_1 R_1 D_1\phi_1 + \gamma_{10}R_1 + \frac{3}{4}\lambda_{10}R_1^3\Big)\sin(\phi_1)\Big)\sin(\omega_1 T_0) + \gamma_{10}R_2\sin(\phi_2)\sin(\omega_2 T_0) \tag{40}$$

$$D_0^2 q_{21} + \omega_2^2 q_{21} = -\frac{1}{4}\lambda_{20} R_2^3 \cos(3\omega_2 T_0 - 3\phi_2) + \Big(-\omega_2(2D_1R_2 + \mu_{20}R_2)\sin(\phi_2) - \Big(2\omega_2 R_2 D_1\phi_2 + \gamma_{20}R_2 + \frac{3}{4}\lambda_{20}R_2^3\Big)\cos(\phi_2)\Big)\cos(\omega_2 T_0) + \gamma_{20}R_1\cos(\phi_1)\cos(\omega_1 T_0) + \Big(\omega_2(2D_1R_2 + \mu_{20}R_2)\cos(\phi_2) - \Big(2\omega_2 R_2 D_1\phi_2 + \gamma_{20}R_2 + \frac{3}{4}\lambda_{20}R_2^3\Big)\sin(\phi_2)\Big)\sin(\omega_2 T_0) + \gamma_{20}R_1\sin(\phi_1)\sin(\omega_1 T_0)$$

The resonance picture appears whether $\omega_1 = \Omega - \varepsilon\chi_1$, $\omega_2 = \Omega - \varepsilon\chi_2$. In order to avoid secularity conditions, the coefficients of terms proportional to $\cos(\Omega T_0)$ and $\sin(\Omega T_0)$ will be zero, leading to the following couple of equations:

$$\begin{aligned}
&2\omega_1 D_1 R_1 + \omega_1\mu_{10}R_1 + \gamma_{10}R_2\sin(\phi_2 - \phi_1 - (\chi_1+\chi_2)T_1) - A_0 sin(\phi_1 + \chi_1 T_1) = 0\\
&2\omega_1 R_1 D_1\phi_1 + \gamma_{10}R_1 + \frac{3}{4}\lambda_{10}R_1^3 - \gamma_{10}R_2\cos(\phi_2 - \phi_1 - (\chi_1+\chi_2)T_1) - A_0 cos(\phi_1 + \chi_1 T_1) = 0\\
&2\omega_2 D_1 R_2 + \omega_2\mu_{20}R_2 - \gamma_{20}R_1\sin(\phi_2 - \phi_1 + (\chi_1+\chi_2)T_1) = 0\\
&2\omega_2 R_2 D_1\phi_2 + \gamma_{20}R_2 + \frac{3}{4}\lambda_{20}R_2^3 - \gamma_{20}
\end{aligned} \tag{41}$$

The stationary solution is obtained if and only if: $D_1R_1 = D_1R_2 = 0$, and the phase is constant, that is to say $D_1\phi_2 - D_1\phi_1 = (\chi_1 + \chi_2)$ et $D_1\phi_2 - D_1\phi_1 = -(\chi_1 + \chi_2)$, $D_1\phi_1 = -\chi_1$. We thus find $D_1\phi_2 = \chi_2$, $D_1\phi_1 = -\chi_1$, et $\chi_2 = -\chi_1$.

Leading to:

$$\begin{aligned}
&\omega_1\mu_{10}R_1 + \gamma_{10}R_2\sin(\phi_2 - \phi_1) - A_0 sin(\phi_1 + \chi_1 T_1) = 0\\
&(-2\omega_1\chi_1 + \gamma_{10})R_1 + \frac{3}{4}\lambda_{10}R_1^3 - \gamma_{10}R_2\cos(\phi_2 - \phi_1) - A_0 cos(\phi_1 + \chi_1 T_1) = 0\\
&\omega_2\mu_{20}R_2 - \gamma_{20}R_1\sin(\phi_2 - \phi_1) = 0\\
&(2\omega_2\chi_2 + \gamma_{20})\,R_2 + \frac{3}{4}\lambda_{20}R_2^3 - \gamma_{20}R_1\cos(\phi_2 - \phi_1)
\end{aligned} \tag{42}$$

The last two lines of Equation (42) give after combination:

$$R_1 = \pm\frac{R_2}{\gamma_{20}}\sqrt{\omega_2^2\mu_{20}^2 + \Big((2\omega_2\chi_2 + \gamma_{20}) + \frac{3}{4}\lambda_{20}R_2^2\Big)^2}, \tan(\phi_2 - \phi_1) = \frac{\omega_2\mu_{20}}{(2\omega_2\chi_2 + \gamma_{20}) + \frac{3}{4}\lambda_{20}R_2^2} \tag{43}$$

Combining the first two lines, we have:

$$\begin{aligned} A_0^2\gamma_{20}^2R_1^2 = {} & (\gamma_{20}\omega_1\mu_{10}R_1^2+\gamma_{10}\omega_2\mu_{20}R_2^2)^2 \\ & +\left(\gamma_{20}(-2\omega_1\chi_1+\gamma_{10})\,R_1^2+\frac{3}{4}\gamma_{20}\lambda_{10}R_1^4\right. \\ & \left.-\gamma_{10}R_2^2\left((2\omega_2\chi_2+\gamma_{20})+\frac{3}{4}\lambda_{20}R_2^2\right)\right)^2 \end{aligned} \tag{44}$$

Equation (35) can be expanded taking into account Equation (33) to give:

$$p_0R_2^{10}+p_2R_2^8+p_4R_2^6+p_5R_2^5+p_6R_2^4+p_7R_2^3+p_8R_2^2+p_9R_2+p_{10}=0, \tag{45}$$

With

$$p_0=\frac{81}{1024\gamma_{20}^3}\lambda_{20}^4(4\gamma_{20}\omega_1^2\mu_{10}^2+3\lambda_{10}),p_2=\frac{27}{64\gamma_{20}^3}\lambda_{20}^3(4\gamma_{20}\omega_1^2\mu_{10}^2+3\lambda_{10})(2\omega_2\chi_2+\gamma_{20})$$

$$p_4=\frac{9}{32\gamma_{20}^3}\lambda_{20}^2(4\gamma_{20}\omega_1^2\mu_{10}^2+3\lambda_{10})(3(2\omega_2\chi_2+\gamma_{20})^2+\omega_2^2\mu_{20}^2)+\frac{9}{8\gamma_{20}}\lambda_{20}^2\omega_1\mu_{10}\gamma_{10}\mu_{20}\omega_2$$

$$p_5=-\frac{9}{16}\gamma_{10}\lambda_{20}^2,$$

$$p_{61}=\frac{3}{4\lambda_{20}^3}\lambda_{20}\omega_2(4\gamma_{20}\omega_1^2\mu_{10}^2+3\lambda_{10})(8\chi_2^3\omega_2^2+2\chi_2\omega_2^2\mu_{20}^2+\omega_2\mu_{20}^2\gamma_{20}+12\omega_2\chi_2^2\gamma_{20}+6\chi_2\gamma_{20}^2)$$

$$p_{63}=\left(-\frac{9}{8\lambda_{20}}\omega_1\chi_1-\frac{9}{16}A_0^2+\frac{9}{16\gamma_{20}}\gamma_{10}\right)\lambda_{20}^2+\left(\frac{9}{4}\gamma_{10}+3\gamma_{20}\omega_1^2\mu_{10}^2\right)\lambda_{20} \tag{46}$$

$$p_{83}=2\omega_1\mu_{10\gamma_{10}\omega_2(4\chi_2\omega_2+\gamma_{20})\mu_{20}}+\mu_{20}^2\omega_2^2\gamma_{10}^2+8\omega_2\omega_1^2\mu_{10}^2\chi_2\gamma_{20}-3\omega_2(A_0^2\lambda_{20}-2\lambda_{10})\chi_2-\frac{3\omega_2\lambda_{20}(-\gamma_{10}+2\omega_1\chi_1)\chi_2}{\gamma_{20}}$$

$$p_{81}=\frac{3}{4}\gamma_{20}\lambda_{10}+\frac{3}{2}\gamma_{10}\lambda_{20}-\frac{3}{2}A_0^2\gamma_{20}\lambda_{20}+\gamma_{20}^2\omega_1^2\mu_{10}^2-3\omega_1\chi_1\lambda_{20},p_8=p_{81}+p_{82}+p_{83}$$

$$p_9=-\gamma_{10}\left(\gamma_{20}+2\chi_{2\omega_2}\right)^2$$

$$p_{10}=-\frac{(\gamma_{20}^2+4\omega_2^2\chi_2^2+4\omega_2\chi_2\gamma_{20}+\omega_2^2\mu_{20}^2)(A_0^2\gamma_{20}+2\omega_1\chi_1-\gamma_{10})}{\gamma_{20}}$$

Equation (45) is the 10th order polynomial equation, which is numerically solved, and the results found are plotted in **Figures 3–6** for some choice of parameters, proving the complexity of the system.

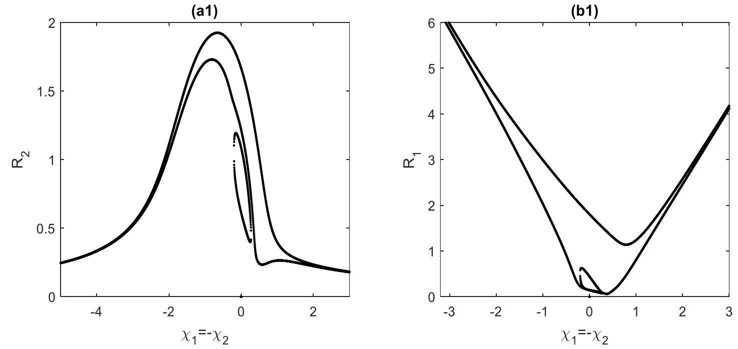

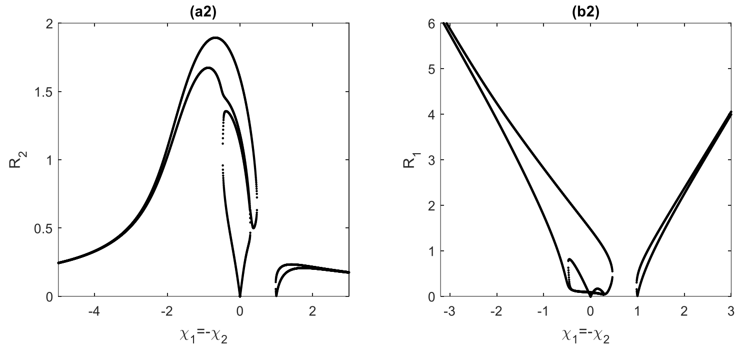

Figure 3. Amplitude of the solution obtained for: $\omega = 1$, $\gamma_{10} = \gamma_{20} = 1$, $\lambda_{10} = \lambda_{20} = -1$, $\mu_{10} = \mu_{20} = 0.05$, (**a1**) $A_0 = 0.5$, (**b1**): $A_0 = 1$, showing the hysteresis. In (**a2**) and (**b2**), one has the quenching for $0.5 < \chi_1 = -\chi_2 < 1$.

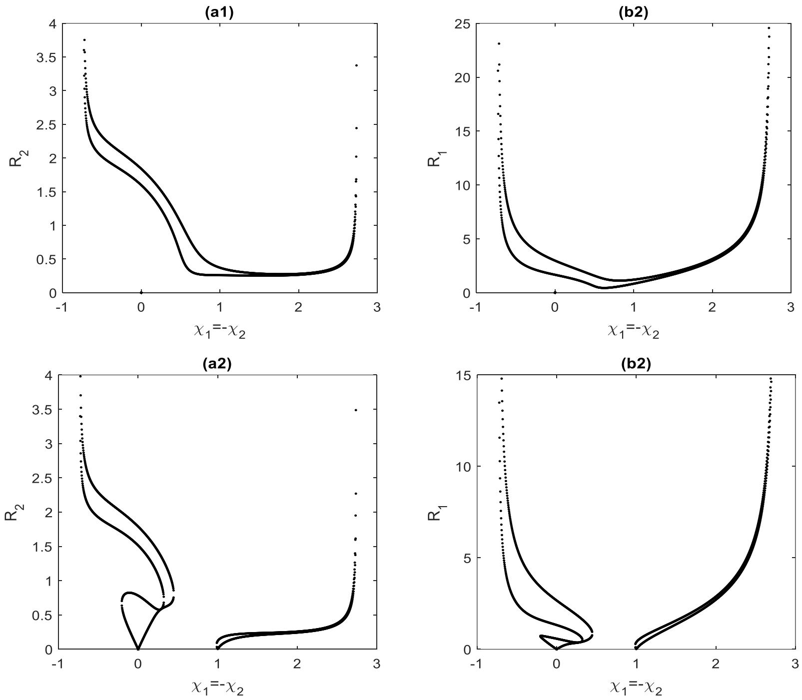

Figure 4. Amplitude of the solution obtained for: $\omega = 1, \gamma_{10} = \gamma_{20} = 1, \lambda_{10} = \lambda_{20} = -1, \mu_{10} = \mu_{20} = 0.5$, (**a1**) $A_0 = 0.5$, (**b1**) $A_0 = 1$, showing the hysteresis. In (**a2**) and (**b2**), one has the quenching for $0.5 < \chi_1 = -\chi_2 < 1$.

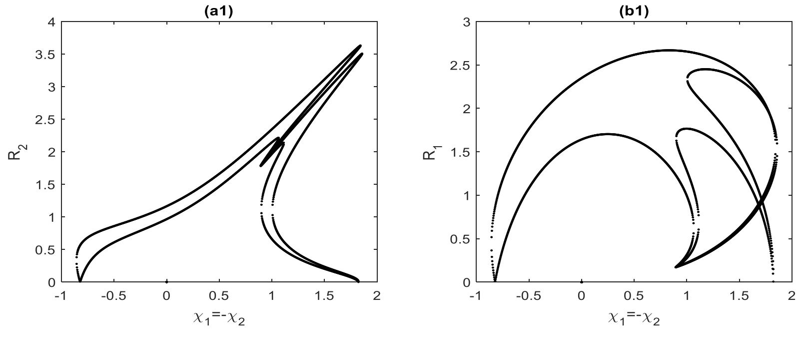

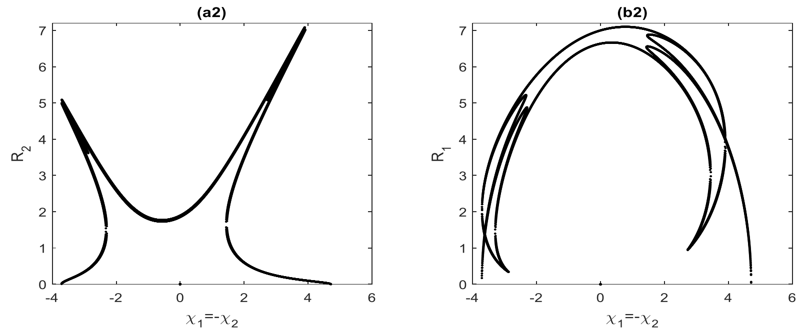

Figure 5. Amplitude of the solution obtained for $\omega = 1, \gamma_{10} = \gamma_{20} = 1, \lambda_{10} = \lambda_{20} = 1, \mu_{10} = \mu_{20} = 0.05$; (1) $A_0 = 2$, (2): $A_0 = 6$, showing the hysteresis.

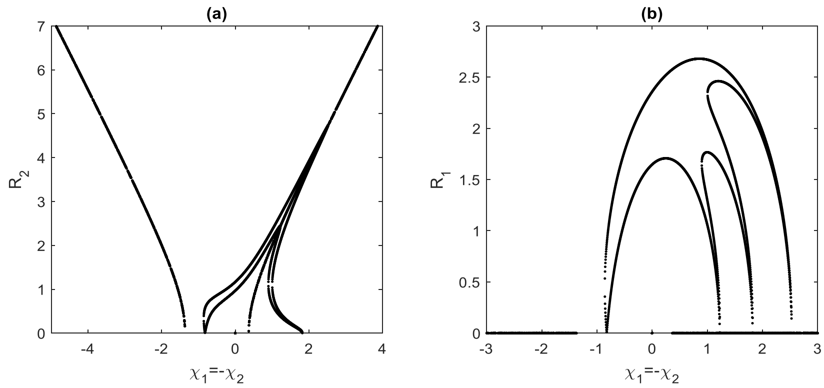

Figure 6. Amplitude of the solution obtained $\omega = 1, \gamma_{10} = \gamma_{20} = 1, \lambda_{10} = \lambda_{20} = 1, \mu_{10} = \mu_{20} = 0.05$; **(a)** $A_0 = 2$, **(b)**: $A_0 = 6$.

3.1.2. Solution for *N*=3

Now for $N = 3$, one has at order ε^0 the set of equations $D_0^2 q_{n0} + \omega_1^2 q_{n0} = 0, n = 1, 2, 3$, which admit as solutions:

$$q_{,n0} = R_n\,(T_1)\cos\big(\omega_{\mathrm{n}} T_0 - \phi_n(T_1)\big)\,, n = 1\,,2,3, \tag{47}$$

At order ε^1 one has:

$$\begin{cases} D_0^2 q_{11} + \omega_1^2 q_{11} = -\mu_{10} D_0 q_{10} - \gamma_{10}(2q_{10} - q_{20} - q_{30}) - 2D_0 D_1 q_{10} - \lambda_{10} q_{10}^3 + A_0 cos(\Omega T_0) \\ D_0^2 q_{21} + \omega_2^2 q_{21} = -2D_0 D_1 q_{20} - \mu_{20} D_0 q_{20} - \gamma_{20}(-q_{10} + 2q_{20} - q_{30}) - \lambda_{20} q_{20}^3 \\ D_0^2 q_{31} + \omega_3^2 q_{31} = -2D_0 D_1 q_{30} - \mu_{30} D_0 q_{30} - \gamma_{30}(2q_{30} - q_{20} - q_{10}) - \lambda_{30} q_{30}^3 \end{cases} \tag{48}$$

By substituting Equation (47) into Equation (48), one obtains by imposing as above the coefficients of the terms proportional to $cos(\Omega\, T_0)$ and $sin(\Omega\, T_0)$ zero the equations, with $\omega_3 = \Omega + \varepsilon\chi_3$, leading to the Equation (53) in the Appendix A. The stationary solution is obtained if and only if $D_1 R_1 = D_1 R_2 = D_1 R_3 = 0$, and the phase is constant, that is to say $D_1\phi_1 = D_1\phi_2 = D_1\phi_3 = 0$, and $\chi_1 = \chi_2 = \chi_3 = 0$. This case corresponds to pure resonance, that is to say $\omega_1 = \omega_2 = \omega_3 = \Omega$.

In order to simplify our investigations here, let us focus on the case where $\phi_1 = \phi_2 = \phi_3$. Equation (48) becomes:

$$\begin{aligned}
&\mu_{10}R_1\omega_1 = A_0 sin(\phi_1)\\
&\mu_{20}R_2\omega_2 = 0\\
&\mu_{30}\omega_3 R_3 = 0\\
&2\gamma_{10}R_1 - A_0 cos(\phi_1) - \gamma_{10}(R_2+R_3) + \frac{3}{4}\lambda_{10}R_1^3 = 0\\
&2\gamma_{20}R_2 + \frac{3}{4}\lambda_{20}R_2^3 - \gamma_{20}(R_1+R_3) = 0\\
&2\gamma_{30}R_3 - \gamma_{30}(R_2+R_1) + \frac{3}{4}\lambda_{30}R_3^3 = 0
\end{aligned} \tag{49}$$

Thus the last equation leads to:

$$R_1 = 2R_3 - R_2 + \frac{3}{4}\frac{\lambda_{30}}{\gamma_{30}}R_3^3 \tag{50}$$

and the last but one equation gives: $R_2 + \frac{\lambda_{20}}{4\gamma_{20}}R_2^3 - R_3 - \frac{\lambda_{30}}{4\gamma_{30}}R_3^3 = 0$, which allows to have:

$$R_2 = \left(\frac{2\gamma_{20}}{\lambda_{20}}\left(R_3 + \frac{\lambda_{30}}{4\gamma_{30}}R_3^3\right) + \sqrt{\frac{4\gamma_{20}^2}{\lambda_{20}^2}\left(R_3 + \frac{\lambda_{30}}{4\gamma_{30}}R_3^3\right)^2 + \frac{64\gamma_{20}^3}{27\lambda_{20}^3}}\right)^{1/3} \exp\left(\frac{in\pi}{3}\right) + \left(\frac{2\gamma_{20}}{\lambda_{20}}\left(R_3 + \frac{\lambda_{30}}{4\gamma_{30}}R_3^3\right) - \sqrt{\frac{4\gamma_{20}^2}{\lambda_{20}^2}\left(R_3 + \frac{\lambda_{30}}{4\gamma_{30}}R_3^3\right)^2 + \frac{64\gamma_{20}^3}{27\lambda_{20}^3}}\right)^{1/3} \exp\left(-\frac{in\pi}{3}\right), \text{ avec n=0,1,2.} \tag{51}$$

The first two equations give:

$$A_0^2 = \mu_{10}^2\omega_1^2R_1^2 + \left(2\gamma_{10}R_1 - \gamma_{10}(R_2+R_3) + \frac{3}{4}\lambda_{10}R_1^3\right)^2. \tag{52}$$

Solving the system of Equation (50)–(52) gives the amplitude of the system as plotted in **Figures 7–9**.

3.2. Numerical investigations

In this subsection, we numerically solve the set of equations of the system given by Equation (29), $f(t) = q_0 \sin(\Omega_n t)$, with $\Omega_n = \frac{n\pi}{L}v$, and $A_0 = \frac{2P_0}{m_i\int_0^L \varphi_i^2(x)dx}$. To this end, the fourth-order Runge Kutta scheme is used, with the initial condition $q_{n0} = 0$, $n = 1, 2, \ldots, N$, with the following parameters kept constant: $\omega_1 = \omega_2 = 0.05, \gamma_1 = 0.25, \lambda_1 = 0.25, \lambda_0 = 1, \mu_1 = 0.01, \mu_2 = 0.05$, $A_0 = 2$.

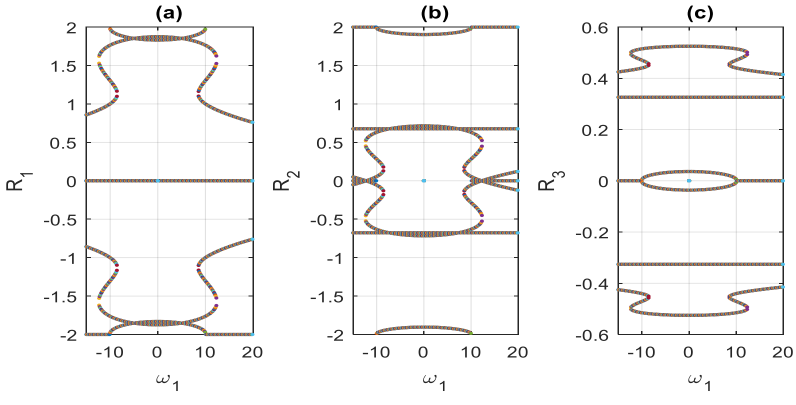

Figure 7. Amplitude of the solution obtained for $N = 3$ and for $\gamma_{10} = \gamma_{20} = \gamma_{30} = 1$, $\lambda_{10} = \lambda_{20} = -\lambda_{30} = 1$, $\mu_{10} = \mu_{20} = \mu_{30} = 0.05$; (1) $A_0 = 1$, (2): $A_0 = 6$.

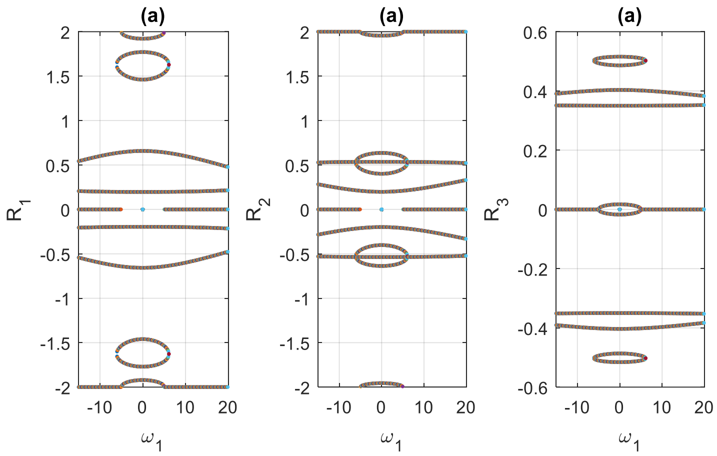

Figure 8. Amplitude of the solution obtained for $N = 3$ and for $\gamma_{10} = \gamma_{20} = \gamma_{30} = 1$, $\lambda_{10} = \lambda_{20} = -\lambda_{30} = 1$, $\mu_{10} = \mu_{20} = \mu_{30} = 0.05$; $A_0 = 0.5$.

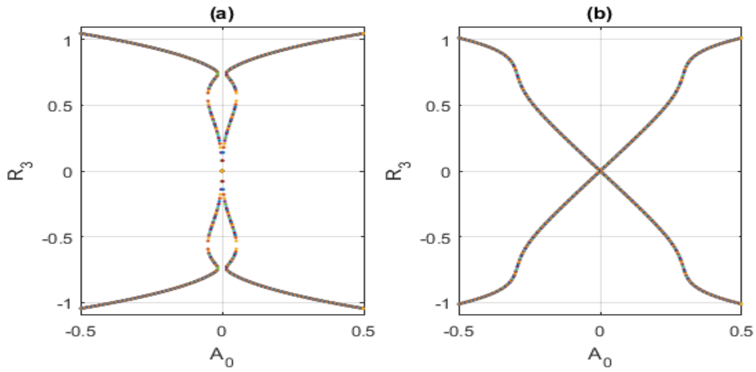

Figure 9. Amplitude of the solution obtained for $N = 3$ and for $\gamma_{10} = \gamma_{20} = \gamma_{30} = 1$, $\lambda_{10} = \lambda_{20} = -\lambda_{30} = 1$, $\mu_{10} = \mu_{20} = \mu_{30} = 0.05$; (**a**): $\omega_1 = 0.5$; (**b**): $\omega_1 = 10$.

3.2.1. Result for *N* = 2

Case for $\omega = 0.5$

Firstly, the bifurcation diagram is plotted as shown in **Figure 10** (and in its zoom given in **Figure B1** of Appendix B) in order to investigate the transition of the system to chaos, while the maximum Lyapunov exponent is plotted to indicate whether the system is chaotic or not, with the parameter γ_2 chosen as the tuning parameter. Thus, **Figure 10a**,**b** shows the bifurcation diagram obtained for $\omega = 0.5$, from where it is obvious that one has the periodic behavior for $0.22 \leq \gamma_2 \leq 0.4$, and $\gamma_2 > 0.88$. For $\gamma_2 < 0.22$, and $\gamma_2 > 0.88$, one has the crisis, with some chaotic windows inside the regular band. **Figure 10c** shows the corresponding maximum Lyapunov exponent, which is in agreement with the bifurcation diagram. **Figure B1** in the Appendix shows zooms of **Figure 10**, used to carry emphasis on the transition of the system.

To justify the behavior of the system, the time trace, the phase portraits, and the frequency spectrum of the system are plotted for some values of γ_2. In **Figure 11**, one has in (a) the temporal evolution of the displacement, (b) the phase portrait, and (c), the frequency spectrum obtained for the same parameters as in **Figure 10**, but with $\gamma_2 = -0.15$. As one can see, one has the chaotic impulses, which are justified by the frequency phase spectrum, which has large a band. In **Figures 12** and **13** obtained for the same parameters as in **Figure 10**, but with $\gamma_2 = 0.2$ and $\gamma_2 = 0.7$, respectively, one has the train of regular impulses, which is justified by their frequency phase spectrum, with a finite number of picks.

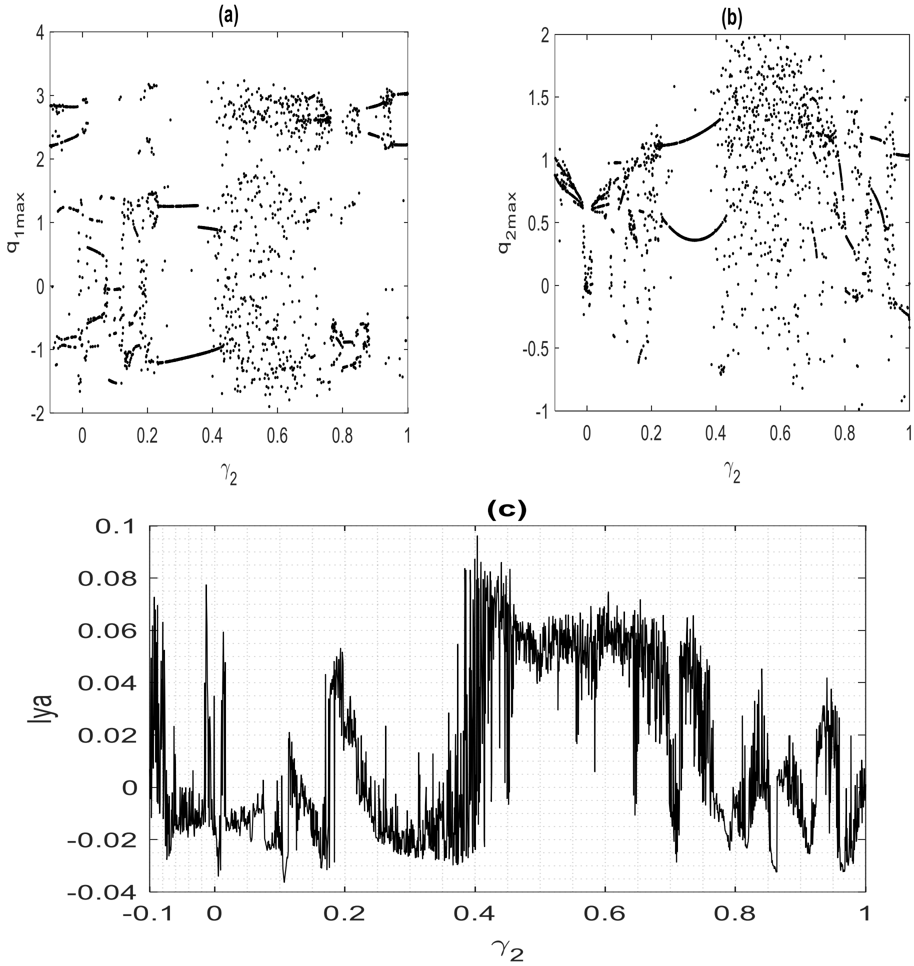

Figure 10. (a,b) Bifurcation diagrams at positions 1 and 2 respectively; **(c)** maximum Lyapunov exponent obtained for $\omega_1 = \omega_2 = 0.05$, $\gamma_1 = 0.25$, $\gamma_2 = -0.17$, $\lambda_1 = 0.25$, $\lambda_2 = 1$, $\mu_1 = 0.01$, $\mu_2 = 0.05$, $A = 2$, $\omega = 0.5$.

Case for weak frequency $\omega = 0.05$

The bifurcation diagram is first plotted as shown in **Figure 14**, for parameters chosen as in **Figure 10**, but with $\omega = 0.05$, which shows the bifurcation picture different to that obtained above in **Figure 10**. In this figure, the chaotic band has considerably reduced, with chaos appearing around $\gamma_2 = 0.5$ and also for $\gamma_2 > 0.85$. **Figures 15** and **16** show the evolution of the system for $\gamma_2 = 0.2$, and $\gamma_2 = 0.5$, respectively, which are the train of bursting signals.

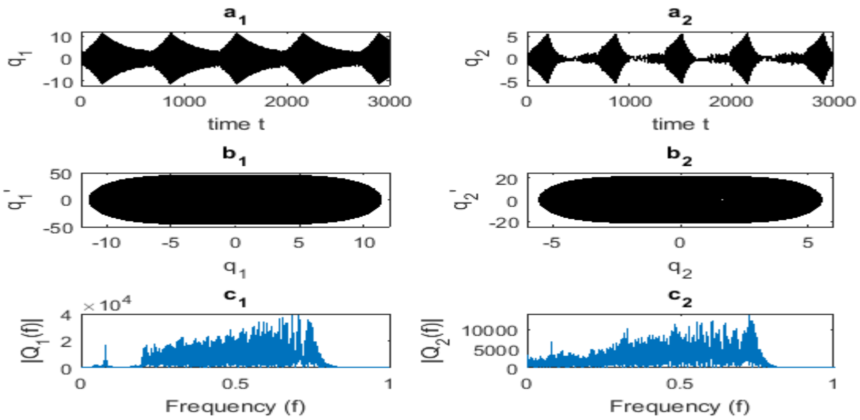

Figure 11. (a) Temporal evolution of the displacements; **(b)** phase portrait; **(c)** frequency spectrum obtained for the same parameters as in **Figure 10**, but with $\gamma_2 = -0.15$. As one can see, one has the chaotic impulses.

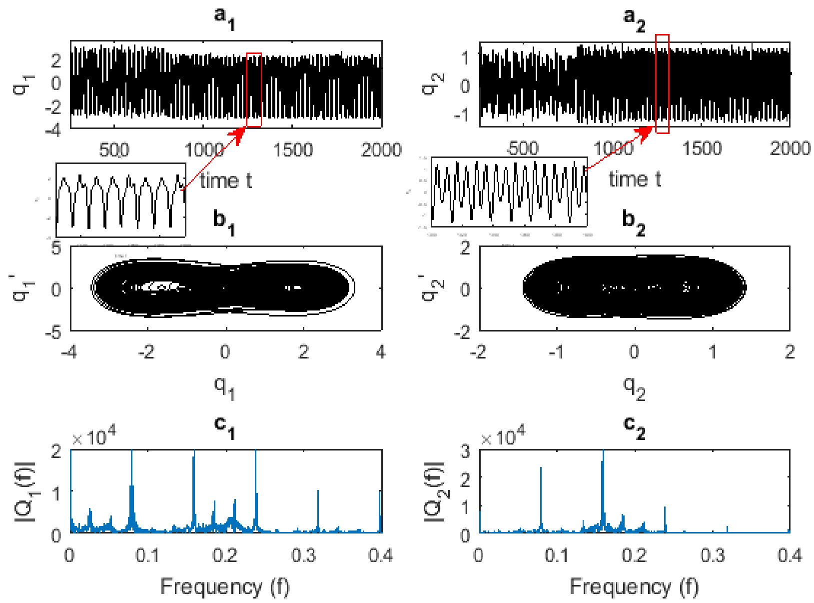

Figure 12. (**a**) Temporal evolution of the displacements, (**b**) phase portrait; (**c**) frequency spectrum obtained for the same parameters as in **Figure 10**, but with $\gamma_2 = 0.2$. As one can see, one has the train of impulses

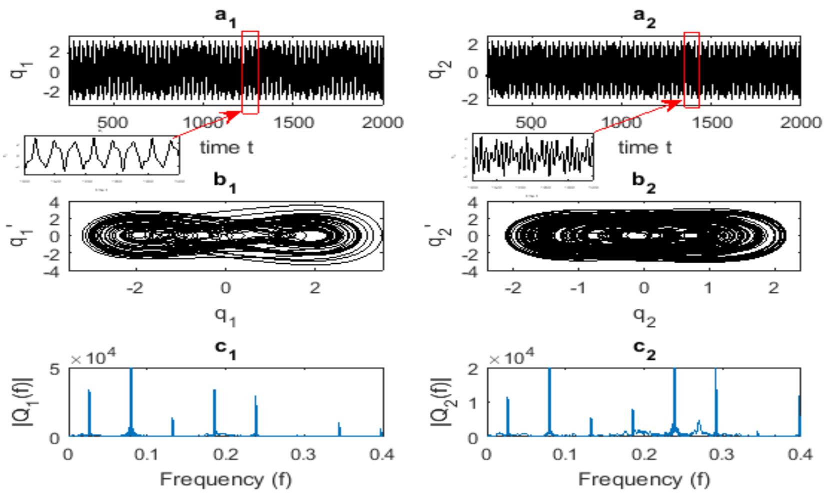

Figure 13. (a) Temporal evolution of the displacements; **(b)** phase portrait; **(c)** frequency spectrum obtained for the same parameters as in **Figure 10**, but with $\gamma_2 = 0.7$. As one can see, one has the train of impulses.

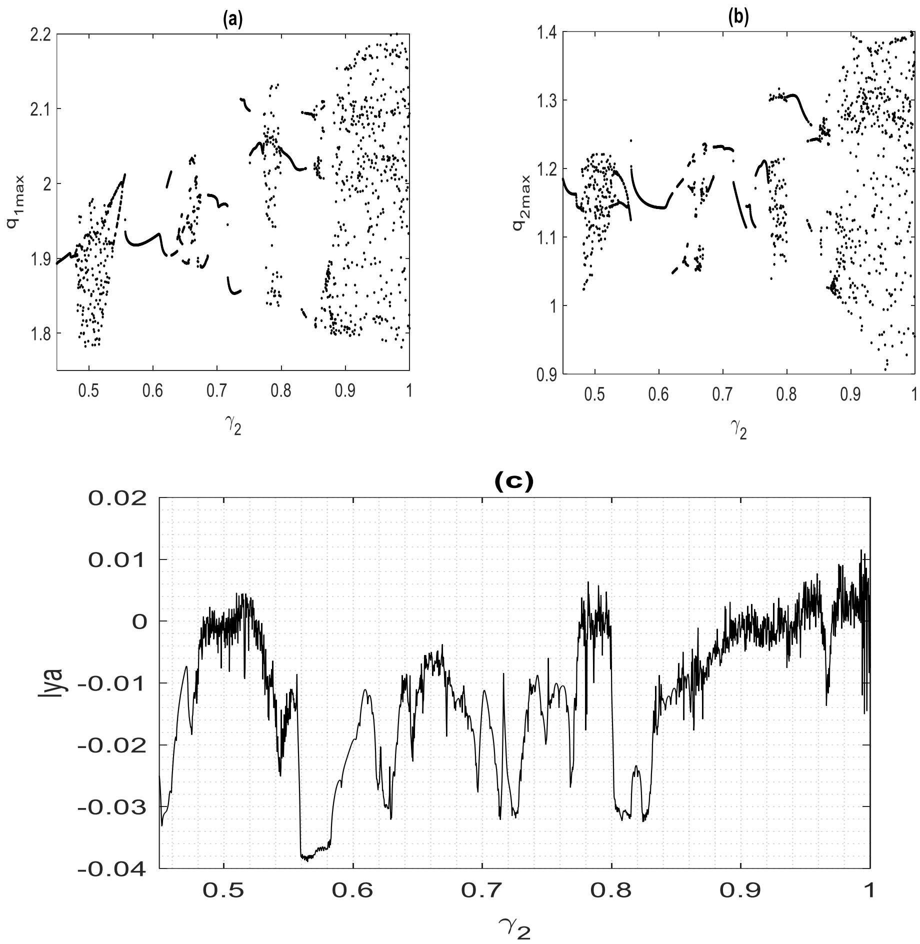

Figure 14. (a,b) Bifurcation diagrams, **(c)** maximum Lyapunov exponent, obtained for $\omega_1 = \omega_2 = 0.05$, $\gamma_1 = 0.25$, $\gamma_2 = -0.17$, $\lambda_1 = 0.25$, $\lambda_2 = 1$, $\mu_1 = 0.01$, $\mu_2 = 0.05$, $A = 2$ and, $\omega = 0.05$.

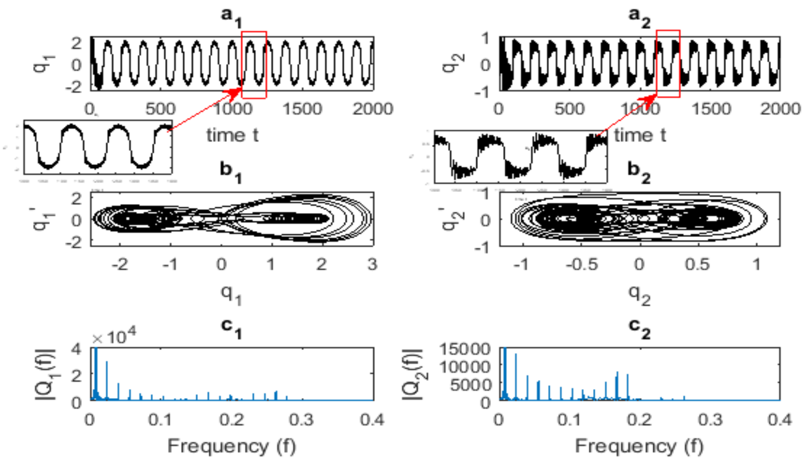

Figure 15. (a) Temporal evolution of the displacements; **(b)** phase portraits; **(c)** frequency spectrums obtained for the same parameters as in **Figure 14**, but with γ_2 = 0.2. As one can see, one has the train of bursting.

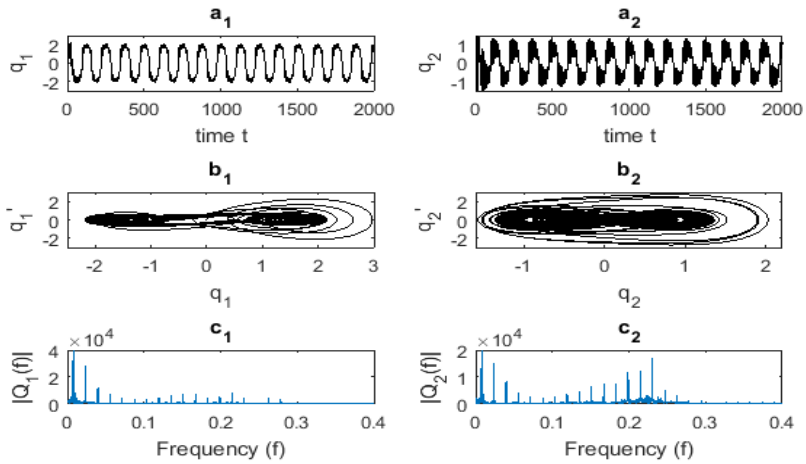

Figure 16. (a) Temporal evolution of the displacements; **(b)** phase portraits; **(c)** frequency spectrums obtained for the same parameters as in **Figure 14**, but with γ_2 = 0.5. One has the train of bursting.

Synchronization

In order to study the synchronization of two consecutive layers, q_2 is plotted as a function of q_1 for the above-studied cases as shown in **Figure 17**. In **Figure 17a**,**b** obtained for $\omega = 0.5$ and $\gamma_2 = -0.15$ and $\gamma_2 = 0.2$, q_2 doesn't synchronize q_1, and the figures obtained look like the chaotic signal, while for (c) and (d), obtained for ($\omega = 0.5$ and $\gamma_2 = 0.7$) and ($\omega = 0.05$ and $\gamma_2 = 0.45$), q_2 synchronizes fairly q_1.

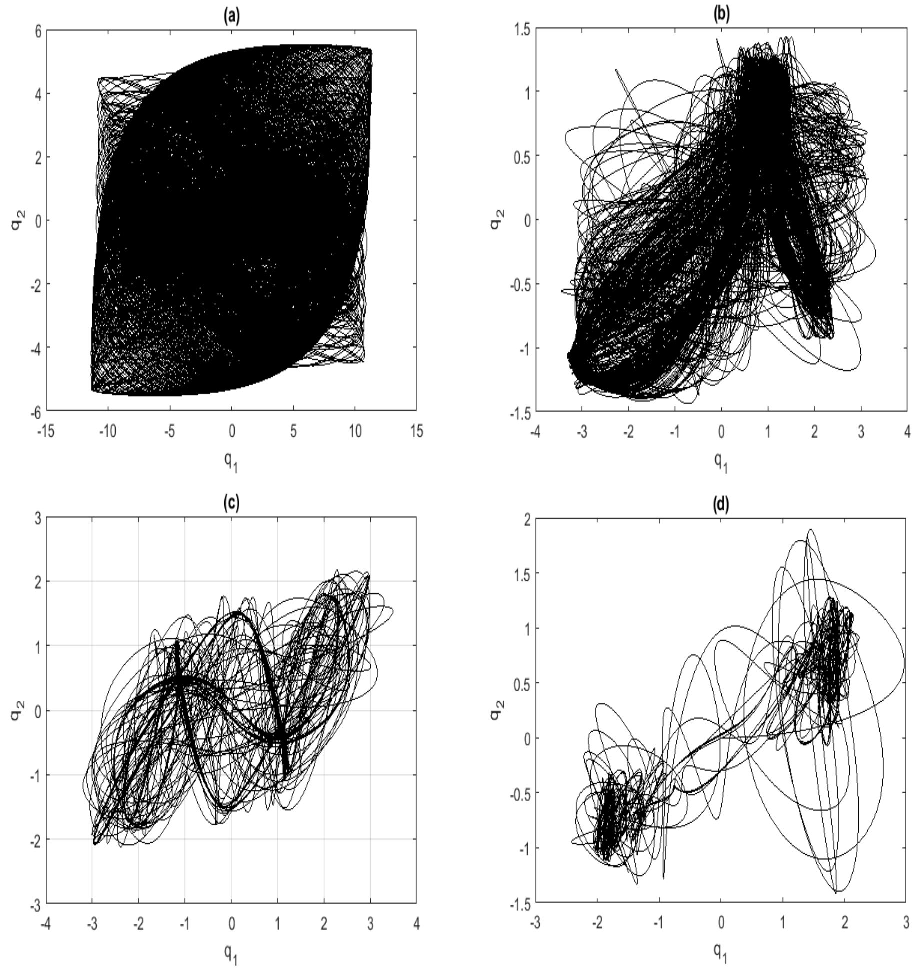

Figure 17. Synchronization curves for (**a**): $\omega = 0.5$ and $\gamma_2 = -0.15$, (**b**): $\omega = 0.5$ and $\gamma_2 = 0.2$; (**c**):$\omega = 0.5$ and $\gamma_2 = 0.7$; (**d**): $\omega = 0.05$ and $\gamma_2 = 0.5$.

3.2.2. Results for *N* = 3

In this case, **Figures 18** and **19** show the behavior of the system for N=3, and for $\omega_1 = 0.05$, $\omega_2 = 1$, $\lambda_1 = 0.25$, $\lambda_2 = 0.5$, $\lambda_3 = 0.5$, $\mu_1 = \mu_3 = 0.01$, $\mu_2 = 0.05$, $\gamma_1 = 0.25$, $\gamma_1 = 0.25$, $\gamma_2 = 0.2$, $\gamma_3 = 0.5$ and $A_0 = 1, \omega = 0.05$ is for **Figure 18**, while $\omega = 0.5$ is for **Figure 19**.

3.3. Discussion

From the above results, it is obvious that by taking into account the effect of nonlinearity of multilayer beam structures on elastic foundations under mobile point loading, the system has rich dynamics depending on both the nature of the system (coupling) and loadings, which means that:

- The dynamics of the system can be chaotic or regular for large frequency values, that is to say, the high speeds of the mobile load. This assertion is in agreement with the results of Shaohua Li et al. [40], who showed that road vibrations excited by moving vehicle loads move from transient chaos to attenuated periodic motion and finally disappear to increase road life. Thus, the chaotic appearance observed shows that throughout the foundation the differential settlement is not uniform; therefore, special treatment of the soil is necessary (clearing, use of synthetic geomembrane, avoidance of preferred isolated and continuous footings, etc.) to reduce the risk of structural collapse.

- The observed crisis (intermittency of chaos) on the bifurcation curves for certain frequency values could be the cause of the destruction of certain foundations and must be considered by engineers when sizing structures and calculating reinforcement.
- The chaotic appearance observed in the soil foundation can also be interpreted as the transition of the soil from the elastic state to the plastic state, which directly affects the physical properties of the soil, such as bulk density, strength, stress, and porosity. However, this chaos could be important for the compaction of the subgrade in road constructions since it could increase the compaction rate.

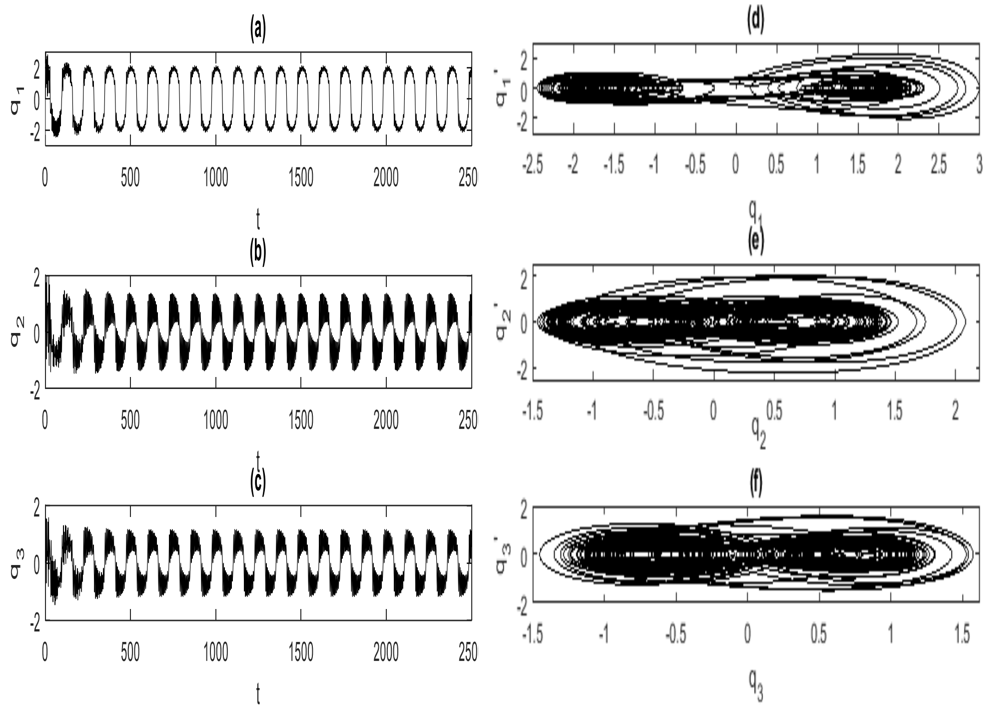

Figure 18. (a,b,c) Temporal evolution of the displacements for N = 3; (**d**,**e**,**f**) phase portraits obtained for $\omega_1 = 0.05$, $\omega_2 = 1$, $\lambda_1 = 0.25$, $\lambda_2 = 0.5$, $\lambda_3 = 0.5$, $\mu_1 = \mu_3 = 0.01$, $\mu_2 = 0.05$, $\gamma_1 = 0.25$, $\gamma_1 = 0.25$, $\gamma_2 = 0.2$, $\gamma_3 = 0.5$ and $A_0 = 1$ and $\omega = 0.05$.

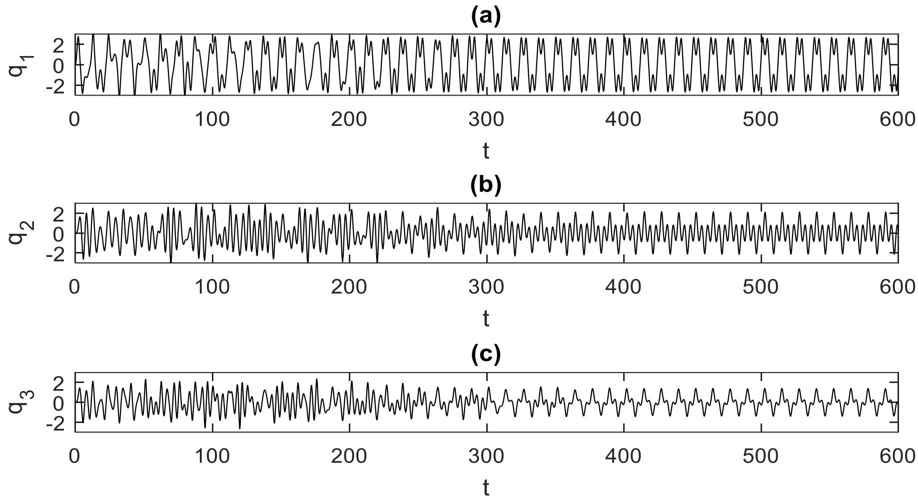

Figure 19. Temporal evolution of the displacements for N = 3 obtained for same parameters as in **Figure 18**, but with ω = 0.5.

4. Conclusion

The dynamics of a multilayer beam structure system under moving point load was studied with particular emphasis on nonlinearity and the coupling parameter. This study could find direct applications to railways and road transport. To achieve this, we first proposed the model studied, taking into account the literature and real physical phenomena. Subsequently, Lagrange's formulations allowed establishing the nonlinear equations of the system, which are a function of the dissipative and elastic coupling between the different layers of the system. The different forms of energy of the system are thus established, including the kinetic energy and the potential energies of deformation and curvature depending on the elasticity of the system and the nature of its deformation.

These equations were thus used to find the Eigen modes and the natural vibration frequencies of the system. Then, by considering a sinusoidal standing waveform at the spatial part of the system equation, the temporal part was reduced to the coupled third-order nonlinear differential equations, where the first line was forced, while the rail at the position data directly feels the effects of all its direct and indirect neighbors (first, second, third, etc.). These coupled nonlinear equations were used to determine the equilibrium points, and these equations were subsequently solved analytically through the multiple time scale method, which showed more complex dynamics, with the formation of hysteresis when the number of beams increased. The system of coupled nonlinear equations of the system was then solved numerically by means of the fourth-order Runge Kutta scheme, and the transition of the system towards chaos due to nonlinearity was analyzed through the bifurcation diagram and the Lyapunov exponent, which showed strong sensitivity to the coupling parameter as well as the system frequency. The results showed for a 2-layer structure that when the frequency value was high ω = 0.5, there was a periodic behavior for $0.22 \le \gamma_2 \le 0.22$ and $\gamma_2 > 0.88$. For $\gamma_2 < 0.22$ and $\gamma_2 > 0.88$, we had the crisis, with a few chaotic windows inside the regular band. When the frequency was low, that is ω = 0.05 the chaotic band was considerably reduced, with chaos appearing around $\gamma_2 = 0.5$ and also for $\gamma_2 > 0.85$. The time trace showed chaotic pulses and bursting-type behavior for some choices of the coupling parameter. We also note that two successive layers do not synchronize. In the field of railway engineering, the bursting behavior obtained here proves that the rails on a ballast layer, subjected to the action of a moving point load induced by the train, could oscillate around several equilibrium points, and this behavior should be taken into consideration by structural engineers in the design and dimensioning of rails and ballasts, as well as in the choice of materials constituting them.

To improve this work, it would be important to study the chaos controller in order to reduce the chaos in the system (which is not desirable in civil engineering), which could then help civil engineers and geotechnicians to fully understand the behavior of soils under load and to take additional measures during the construction of structures. It would be important to take into account the friction between the adjacent layers as well as between the beam and foundation, which can introduce an additional coupling term proportional to $\left(\frac{\partial}{\partial t}\left(w_i(x,t)\right)-\frac{\partial}{\partial t}\left(w_j(x,t)\right)\right)$ and which is neglected here, but will constitute perspective for future investigations. It would also be important to make real experiments confirming our findings. Works in these lights are now under consideration.

Author contributions: Methodology, RE, MLW and GBN; data analysis, MLW and GBN; validation, HS, FK and SN; formal analysis, FK and SN; investigation, HS, FK and SN; writing—original draft preparation, RE, MLW and GBN; writing—review and editing, RE, GBL, HS, FK and SN. All authors have read and agreed to the published version of the manuscript.

Data availability and materials: All data generated or analyzed during this study are included in this manuscript.

Conflict of interest: The authors declare no conflict of interest.

References

1. Schweizerhof K, Konyukhov A. Some remarks on load modeling in nonlinear structural analysis–Statics with large deformations–Consistent treatment of follower load effects and load control. International journal for numerical methodsin engineering. 2024; 125(11)

2. Eurocode 1. Actions on structures–EN 1991 Part 1.1-1.7 and parts 2-5: General actions as well as e.g. traffic loads on bridges and other civil engineering works. Available online: https://www.phd.eng.br/wp-content/uploads/2015/12/en.1991.2.2003.pdf (accessed on 2 June 2024).
3. Jishnu JK, Chauhan DS, Vundavilli P. Design of Neural Network-Based Adaptive Inverse Dynamics Controller for Motion Control of Stewart Platform. International Journal of Computational Methods. 2022; 19(08): 2142010.
4. Dai L, Jazar RN. Nonlinear Approaches in Engineering Applications, Applied Mechanics, Vibration Control, and Numerical Analysis. Springer; 2015.
5. Neff J, In V, Obra C, et al. Applications of Nonlinear and Reconfigurable Electronic Circuits. In: In V, Longhini P, Palacios A (editors). Understanding Complex Systems. Springer; 2009.
6. Lu HCC. A review of applications of nonlinear dynamics in power electronics systems. Australian Journal of Electrical and Electronics Engineering. 2004; 1(2): 75–81.
7. Zhang DW, Bin SH, You C, et al. Enhancing the nonlinearity of optomechanical system via multiple mechanical modes. Optics Express. 2022; 30(2): 1314–1326.
8. Bano R, Asghar M, Ayub K, et al. Theoretical Perspective on Strategies for Modeling High Performance Nonlinear Optical Materials. Front. Mater. 2021; 8:783239.
9. Iqbal J, Ullah M, Kkan SG, et al. Nonlinear control systems–A brief overview of historical and recent advances. Nonlinear Engineering. 2017; 6(4): 301–312.
10. Al-Nadhari AM, Abderrahmani S, Hamadi D, et al. The efficient geometrical nonlinear analysis method for civil engineering structures. Asian. J. Civ. Eng. 2024; 25: 3565–3573.
11. Tafo JBG, Kenmogne F, Kongne AM, et al. Modulated solitons and transverse stability in a two-dimensional nonlinear reaction diffusion electrical network. Results in Physics. 2023; 50: 106532.
12. Kenmogne F, Noah PMA, Tafo JBG. Stability of modulated signals in the damped mechanical network of discontinuous coupled system oscillators with irrational nonlinearities. Arch. Appl. Mech. 2022; 92: 3077–3091.
13. Li J, Touil I, Lu B, et al. Interfacial shear and elongational rheology of immiscible multi-micro-nanolayered polymers: contribution for probing the effect of highly mismatched viscoelastic properties and modeling interfacial tension properties. Rheologica Acta. 2024; 63(5): 1–17.
14. Li L, Li J, Wang Y, et al. Analysis of nonlinear load-displacement behaviour of pile groups in clay considering installation effects. Soils and Foundation. 2020; 60: 752–766.
15. Moon FC, Johnson MA, Holmes WT. Controlling chaos in a two-well oscillator. International Journal of Bifurcation and chaos. 1996; 6(2): 337–347.
16. Kenmogne F, Noah PMA, Dongmo ED, et al. Effects of Time Delay on the Dynamics of Nonlinear Beam on Elastic Foundation Under Harmonic Moving Load: Chaotic Detection and Its Control. Journal of Vibration Engineering & Technologies. 2021; 10: 2327–2346.
17. Settimi V, Lepidi M, Bacigalupo A. Nonlinear dispersion properties of one-dimensional mechanical metamaterials with inertia amplification. International Journal of Mechanical Sciences. 2021; 201: 106461.
18. Kenmogne F, Wokwenmendam ML, Simo H, et al. Effects of damping on the dynamics of an electromechanical system consisting of mechanical network of discontinuous coupled system oscillators with irrational nonlinearities: Application to sand sieves. Chaos, Solitons and Fractals. 2022;156: 111805.
19. Jiang L, Liu C, Peng L, et al. Dynamic analysis of multi-layer beam structure of rail track system under moving load based on mode decomposition. Journal of Vibration Engineering & Technologies. 2021; 4: 1463–1481.
20. Froio D, Rizzi E, Simões FMF, Costa APD. Dynamics of a beam on a bilinear elastic foundation under harmonic moving load. Acta. Mech. 2018; 229: 4141–4165.
21. Ouzizi A, Abdoun F, Azrar L. Nonlinear dynamics of beams on nonlinear fractional viscoelastic foundation subjected to moving load with variable speed. Journal of Sound and Vibration. 2022; 523: 116730.
22. Soffietti F, Turello D, Pinto F. Pseudo-static Winkler springs for longitudinal underground structures subjected to shear waves. Geomechanics and Geoengineering. 2024; 19(6): 1–22.
23. Gholipour A, Ghayesh MH, Zhang Y. A Comparison between Elastic and Viscoelastic Asymmetric Dynamics of Elastically Supported AFG Beams. Vibration. 2020; 3: 3–17.
24. Lamprea-Pineda AC, Connolly DP, Hussein MF. Beams on elastic foundations–A review of railway applications and solutions. Transportation Geotechnics. 2022; 33: 100696.

25. Son H, Bảy VK, Van Tuong T, et al. Horizontal oscillations of the wood sawing support during the cutting process in a wood sawing line using a vertical band saw. Engineering Solid Mechanics. 2024; 12: 247–258.
26. Nguyen TP, Pham DT, Hoang PH. Effects of foundation mass on dynamic responses of beams subjected to moving oscillators. Journal of Vibroengineering. 2020; 22(2).
27. Sheinman I, Adan M, Altus E,. On the role of the displacement function in nonlinear analysis of beams on an elastic foundation. Thin-Walled Structures. 1993; 15(2): 109–125.
28. Abumandour RM, Eldesoky IM, Safan MA, et al. Deflection of Non-Uniform Beams Resting on a Non-Linear Elastic Foundation Using (GDQM). International Journal of Structural and Civil Engineering Research. 2017; 6(1).
29. Lia X, Zhub M, Zhanga B, et al. A review of artificial intelligence applications in high-speed railway systems. High-speed Railway. 2014; 2: 11–16.
30. Train on the railway track. Available online: https://www.theeastafrican.co.ke/tea/business/kenyan-government-to-spend-731m-on-new-trains-4230714 (accessed on 15 January 2023).
31. Abumandour RM, Eldesoky IM, Safan MA, et al. Vibration Analysis of Non-uniform Beams Resting on Two Layer Elastic Foundations Under Axial and Transverse Load Using (GDQM). International Journal of Mechanical Engineering and Applications. 2017; 5(2).
32. Awodola TO, Omolofe B. Flexural motion of elastically supported rectangular plates under concentrated moving masses and resting on bi-parametric elastic foundation. J. Vib. Eng. Technol. 2018; 6: 165–177.
33. Rezvykh A. Road construction Western Europe- Western China. The Caterpillar Vibrating Tandem Compactor Flatteens Asphalt Layers. Alamy; 2012.
34. Kenmogne F, Ouagni MST, Simo H, et al. Effects of time delay on the dynamical behavior of nonlinear beam on elastic foundation under periodic loadings: Chaotic detection and it control. Results in Physics. 2022; 35: 105305.
35. Junker RG, Relan R, Madsen H. Physical-stochastic continuous time identification of a forced Duffing oscillator. ISA Transactions. 2022; 126: 226–234.
36. Salas AH, Abu Hammad M, Alotaibi BM, et al. Analytical and Numerical Approximations to Some Coupled Forced Damped Duffing Oscillators. Symmetry. 2022; 14: 2286.
37. Timesli A. Buckling Behavior of SWCNTs and MWCNTs Resting on Elastic Foundations Using an Optimization Technique. Phys. Mesomech. 2022; 25: 129–141.
38. Mohan A, Kuriakose B. Analysis of beam on elastic foundation. International Journal of Creative Research Thoughts (IJCRT). 2024; 12(1).
39. Salas AHS, Hernández JEC, Hernández LJM. The Duffing Oscillator Equation and its Applications in Physics, Mathematical problem in engineering. Wiley online library; 2021.
40. Abdelrahman AA, Esen I, Daikh AA, et al. Dynamic analysis of FG nanobeam reinforced by carbon nanotubes and resting on elastic foundation under moving load. Mechanics Based Design of Structures and Machines. 2023; 51(10): 5383–5406.

Appendix A

Equations obtained after Equation (48)

$$
\begin{aligned}
&2R_1\omega_1D_1\phi_1 + 2\gamma_{10}R_1 - A_0cos(\phi_1 + T_1\chi_1) \\
&\qquad - \gamma_{10}\big(R_2cos(\phi_1 - \phi_2 + T_1(\chi_1 + \chi_2)) + R_3cos(\phi_1 - \phi_3 + (\chi_1 + \chi_3)T_1)\big) + \frac{3}{4}\lambda_{10}R_1^3 = 0 \\
&2\omega_2D_1R_2 + \mu_{20}R_2\omega_2 - \gamma_{20}\big(R_1sin(\phi_2 - \phi_1 + (\chi_1 + \chi_2)T_1) + R_3sin(\phi_2 - \phi_3 + T_1(\chi_2 + \chi_3))\big) = 0 \\
&2R_2\omega_2D_1\phi_2 + 2\gamma_{20}R_2 + \frac{3}{4}\lambda_{20}R_2^3 - \gamma_{20}(R_1cos(\phi_2 - \phi_1 + T_1(\chi_1 + \chi_2)) + R_3\cos(\phi_2 - \phi_3 + T_1(\chi_2 + \chi_3)) \\
&\qquad = 0 \\
&2\omega_{30}D_1R_3 + \mu_{30}\omega_3R_3 - \gamma_{30}(R_1sin(\phi_3 - \phi_1 + T_1(\chi_1 + \chi_3)) + R_2sin(\phi_3 - \phi_2 + T_1(\chi_2 + \chi_3))) = 0 \\
&2R_3\omega_{30}D_1\phi_3 + 2\gamma_{30}R_3 - \gamma_{30}\big(R_2cos(\phi_3 - \phi_2 + T_1(\chi_2 + \chi_3)) + R_1cos(\phi_3 - \phi_1 + T_1(\chi_1 + \chi_3))\big) + \frac{3}{4}\lambda_{30}R_3^3 \\
&\qquad = 0
\end{aligned}
\tag{A1}
$$

Appendix B

Zooms of the bifurcation diagram showing in Figure 10.

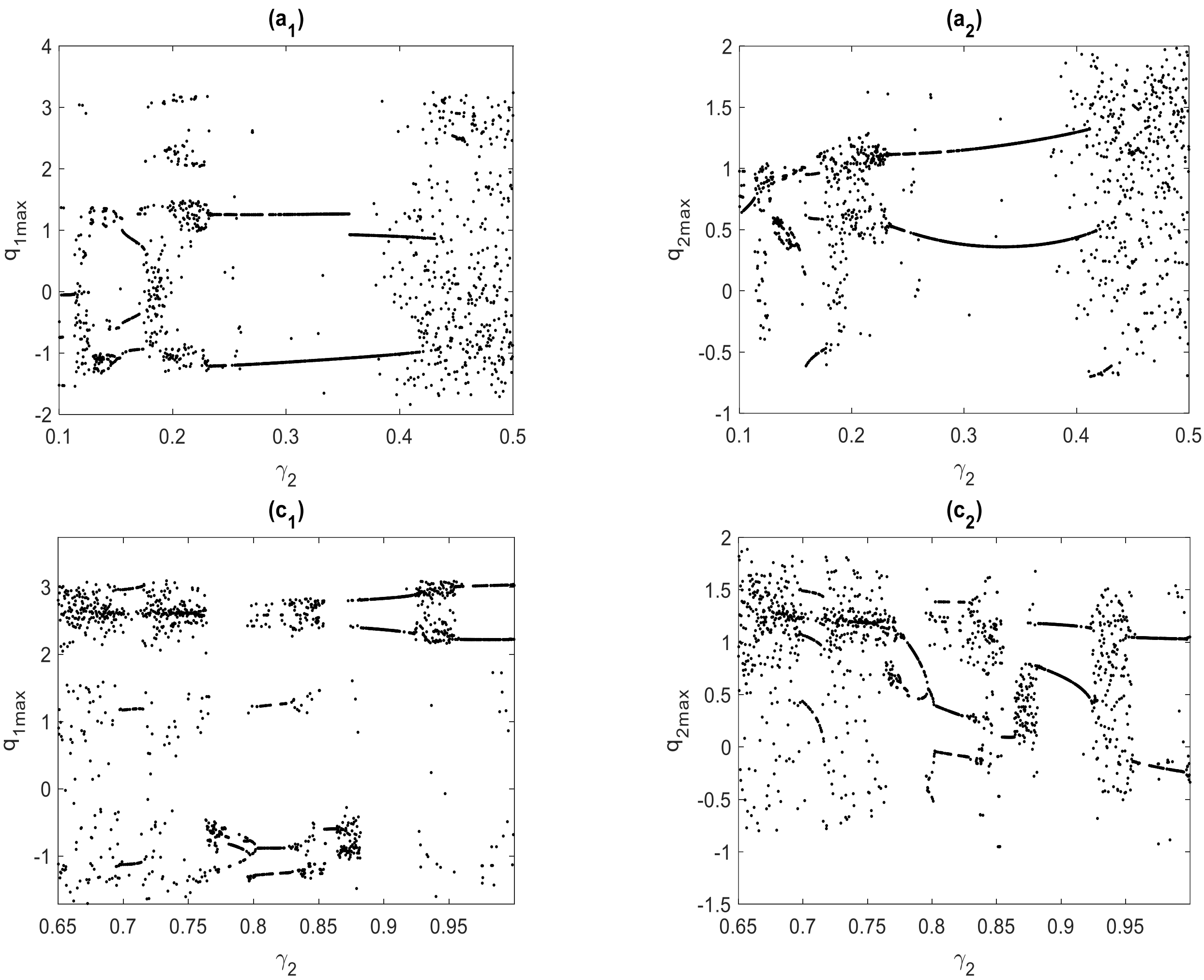

Figure B1. Zooms of the Bifurcation diagram obtained in **Figure 10.**